

A geometrically intrinsic Lagrangian-Eulerian scheme for 2D Shallow Water Equations with variable topography and discontinuous data

Eduardo Abreu^a, Elena Bachini^b, John Pérez^c, Mario Putti^d

^a*Department of Applied Mathematics, University of Campinas, Brazil*

^b*Institute of Scientific Computing, TU Dresden, Germany*

^c*ITM-University Institution, Medellin, Colombia*

^d*Department of Mathematics "Tullio Levi-Civita", University of Padua, Italy*

Abstract

We present a Lagrangian-Eulerian scheme to solve the shallow water equations in the case of spatially variable bottom geometry. Using a local curvilinear reference system anchored on the bottom surface, we develop an effective first-order and high-resolution space-time discretization of the no-flow surfaces and solve a Lagrangian initial value problem that describes the evolution of the balance laws governing the geometrically intrinsic shallow water equations. The evolved solution set is then projected back to the original surface grid to complete the proposed Lagrangian-Eulerian formulation. The resulting scheme maintains monotonicity and captures shocks without providing excessive numerical dissipation also in the presence of non-autonomous fluxes such as those arising from the geometrically intrinsic shallow water equation on variable topographies. We provide a representative set of numerical examples to illustrate the accuracy and robustness of the proposed Lagrangian-Eulerian formulation for two-dimensional surfaces with general curvatures and discontinuous initial conditions.

Keywords: Balance laws on surface, shallow water equations, spatially variable topography, intrinsic Lagrangian-Eulerian scheme, no-flow surfaces

1. Introduction

Partial Differential Equations (PDEs) modeling processes occurring on surfaces have been the subject of several studies in recent years. Typically, the equations governing these processes are developed from their three-dimensional counterparts and letting the dimension normal to the surface go to zero or, alternatively, by averaging the three-dimensional equations along the local normal direction and employing parameter perturbation analysis to impose the condition that the process occurs prevalently along a direction parallel to the surface. Recent examples of these two approaches can be found in [1], where a model for the elastic equilibrium of nematic liquid crystals was derived using the first method, and in [2] where averaging and perturbation analysis are combined to derive the shallow water equations from the Navier-Stokes model for geophysical applications. These approaches are typically employed at wide ranges of scales, from molecular [3, 4, 5] to continental [6, 7, 8, 9, 2] and even planetarial [10, 11]. These phenomena typically act on a surface that can be a material interface such as the cell membrane [3] or the soil-water-atmosphere interface in rivers or lakes [12] or the atmosphere [7], or modeled interfaces such as those arising in density-dependent multi-layer shallow water [13, 14]. In this setting, the curvature of the interface over which the flow occurs, i.e., the bed profile, plays a fundamental role and the governing PDEs must be adapted to the geometrical characteristics of this interface.

In this paper we address Shallow Water (SW) models as used within the context of geophysical flows to simulate fluid flows in natural systems such as rivers, lakes, oceans, and the atmosphere [15, 16, 13, 14]. Only few attempts at including the bed geometry into the SW equations are available [17, 18, 6, 8]. Typically, these approaches yield systems of balance laws that are characterized by non-autonomous flux functions, due to the presence of spatially dependent geometric information [18, 6], and to source terms that contain flux variables.

These two characteristics separately contribute to the difficulties in designing accurate and efficient numerical solvers. The presence of non-autonomous flux functions yields discontinuous local Riemann problems and complicate the identification of the correct wave structure and interaction that is needed in Godunov-type Finite Volume (FV) or Discontinuous Galerkin (DG) discretization approaches (see, e.g., [19, 20, 21, 22, 23]). Most of the approaches used in the presence of discontinuous fluxes are tailored to the specific cases of study and difficulties have been reported to adapt these approaches to general first order monotone schemes [23]. On the other hand, the presence of flux variables in the source term also requires careful treatment, in particular to ensure the well-balance of the discrete equations [24, 14].

Recently, starting from the three-dimensional Navier-Stokes equation, [2] developed a geometrical shallow-water model that is defined on a local reference system anchored on the bottom surface and that uses only intrinsic geometric quantities. The resulting covariant formulation contains intrinsic differential operators, such as divergence and gradients that encapsulate the relevant geometric information. Among the merits of this approach is that it yields a well-posed system of hyperbolic balance laws with forcings that do not contain flux variables. This allows the use of time-splitting to incorporate source terms in the numerical discretization by geometrically intrinsic FV [2] or DG methods [25]. However, the intrinsic flux functions are non-autonomous due to the presence of the metric tensor. This may cause oscillations as reported in [2] where an intrinsic first-order Godunov FV method with HLLC Riemann solver adapted to the geometric setting is proposed. Other attempts to overcome this problem in a simpler geometric setting were reported in [9] where a FORCE-type scheme [26] was used to avoid altogether the use of Riemann Solvers.

The problem of non-autonomous fluxes can be addressed by means of the Lagrangian-Eulerian approach [27, 28, 29, 30, 31, 32, 33, 34]. In fact, in the past decades several papers have introduced different Lagrangian-type methods, for instance semi-Lagrangian methods [35], and arbitrary Lagrangian–Eulerian methods [36]. An important notion on which we base our developments is contained in the work of [37, 38, 39], later considered also by [40, 35]. The original work [37] introduces the Locally Conservative Eulerian–Lagrangian Method (LCELM), which improves the modified method of characteristics introducing a *space-time control volume* where local conservation is enforced. This control volume is essentially an integral tube whose boundaries are no-flow surfaces.

In this work, we start from the geometrically intrinsic approach of [2] and extend the Lagrangian-Eulerian method for hyperbolic systems and balance laws developed in [27, 28, 29, 30, 31, 32, 33, 34] to include geometric effects. In short, the proposed numerical scheme is constructed in two steps. A first Lagrangian evolution step evolves the state from time t^n to t^{n+1} along the space-time control volume appropriately defined to take into consideration also the presence of source terms. The second (Eulerian projection) step averages the evolved solution over the original grid by maintaining local conservation. The fully discrete Lagrangian-Eulerian scheme formulation discussed here is based on the new interpretation of the integral tube, as a Lagrangian no-flow surface [27, 33, 31]. A new aspect of our Lagrangian-Eulerian method that we would like to mention is the dynamic forward tracking of the no-flow surfaces at each time step. This is the key to avoid altogether the use of Riemann solvers and maintain accuracy in the presence of non-autonomous fluxes. Roughly speaking, our method can be viewed as some sort of combination of Godunov-upwinding and Central differencing. An effective improvement over Godunov-upwind schemes is the fact that no Riemann solvers are needed, and thus the time-consuming calculation of the linearized characteristic directions can be avoided. Indeed, as typical of central differencing, the Jacobian matrix of the associated flux functions is neither constructed nor evaluated. The forward tracking reduces numerical dissipation and makes non-oscillatory and high-order reconstructions redundant, thus reducing complexity of the algorithm. In addition, stabilizing numerical viscosity in the proposed approach can be shown to assume the well-known Q -form (see [27]) associated to the underlying numerical flux and satisfies the property that the numerical flux is proportional to the ratio between the time step size and cell diameter. This scalar value is used as an approximation of the local speed of propagation into the space-time control volumes and can be used to define the CFL stability constraint.

The paper is organized as follows. In Section 2, we develop the proposed intrinsic Lagrangian-Eulerian approach. First, the geometrically Intrinsic Shallow Water Equations (ISWE) are re-written in time-space divergence form to adapt to the development of the intrinsic Lagrangian-Eulerian scheme taking into account the geometric properties of the bottom surface. Next, the Lagrangian-Eulerian scheme is developed for

general cell shapes discretizing the surface and it is then further specialized to square cells in Section 3. In this case monotonicity and stability of the scheme can be easily proved. Section 4 reports numerical results on surfaces of different shapes. Finally, Section 5 contains the concluding remarks.

2. Intrinsic Lagrangian-Eulerian Finite Volumes for SWEs

2.1. The geometrically intrinsic SWE flow system

Consider a surface $\Gamma \subset \mathbb{R}^3$ equipped with a metric \mathcal{G} where the system of shallow water equations (SWEs) is defined. The geometrical framework presented in [2] is employed here and extended when needed to handle the system in a Lagrangian-Eulerian approach. The geometrically Intrinsic SWE (ISWE) system can be defined as:

$$\frac{\partial \mathbf{U}}{\partial t} + \nabla_{\mathcal{G}} \cdot \mathbf{F}(\mathbf{s}, \mathbf{U}) = -\mathbf{S}(\mathbf{s}, \mathbf{U}), \quad (1)$$

subject to the Cauchy data:

$$\mathbf{U}(0, s^1, s^2) = \mathbf{U}_0,$$

where $\mathbf{U} = \{\mathbf{U}^\beta\}_{\beta=1}^3 = [\eta, q^1, q^2]^T$ is the conservative variable, with η the depth of the normal fluid and q^i , $i = 1, 2$, the averaged velocity in the two tangential directions. Denoting by $\mathbf{s} = (s^1, s^2)$ the coordinates with respect to a Local Reference System (LCS) anchored on the bottom surface Γ , the differential operators are defined intrinsically with respect to the LCS by careful use of the metric tensor \mathcal{G} related to the \mathbf{s} local coordinates. This is the meaning, for example, of the symbol $\nabla_{\mathcal{G}} \cdot$ in (1) that denotes the intrinsic divergence operator (see appendix Appendix A). The hyperbolic flux function \mathbf{F} and the source term \mathbf{S} can be written intrinsically as:

$$\mathbf{F}(\mathbf{s}, \mathbf{U}) = \begin{bmatrix} q^1 & q^2 \\ \frac{(q^1)^2}{\eta} + \frac{g\eta^2}{2h_1^2} \frac{\partial x^3}{\partial s^3} & \frac{q^1 q^2}{\eta} \\ \frac{q^1 q^2}{\eta} & \frac{(q^2)^2}{\eta} + \frac{g\eta^2}{2h_2^2} \frac{\partial x^3}{\partial s^3} \end{bmatrix} \quad \text{and} \quad \mathbf{S}(\mathbf{s}, \mathbf{U}) = \begin{bmatrix} 0 \\ \frac{g\eta^2}{2h_1^2} \frac{\partial}{\partial s^1} \left(\frac{\partial x^3}{\partial s^3} \right) + \frac{g\eta}{h_1^2} \frac{\partial x^3}{\partial s^1} - \frac{1}{\rho} [\nabla_{\mathcal{G}} \cdot T_{sw}]^{(1,\cdot)} - \frac{\tau_b^1}{\rho} \\ \frac{g\eta^2}{2h_2^2} \frac{\partial}{\partial s^2} \left(\frac{\partial x^3}{\partial s^3} \right) + \frac{g\eta}{h_2^2} \frac{\partial x^3}{\partial s^2} - \frac{1}{\rho} [\nabla_{\mathcal{G}} \cdot T_{sw}]^{(2,\cdot)} - \frac{\tau_b^2}{\rho} \end{bmatrix},$$

where x^3 and s^3 in $\frac{\partial x^3}{\partial s^3}$ indicate the coordinates along the vertical and normal directions, respectively. The tensor T_{sw} is the stress tensor and the functions ρ and τ_b are the density of the fluid and the friction to the bottom, respectively.

Our goal is to develop an Intrinsic Lagrangian-Eulerian approach for this system of intrinsic SWE, starting by defining a *generalized time-space divergence form* for the balance law (1). First, we need to extend the metric tensor in time-space to handle time as an ‘‘intrinsic’’ variable. Thus we define:

$$\mathbb{G} := \left(\begin{array}{c|c} 1 & \\ \hline & \mathcal{G} \end{array} \right) = \begin{pmatrix} 1 & 0 & 0 \\ 0 & \|\mathbf{t}_1(\mathbf{P})\|^2 & 0 \\ 0 & 0 & \|\mathbf{t}_2(\mathbf{P})\|^2 \end{pmatrix} = \begin{pmatrix} 1 & 0 & 0 \\ 0 & h_{(1)}^2 & 0 \\ 0 & 0 & h_{(2)}^2 \end{pmatrix} = \begin{pmatrix} g_{11} & 0 & 0 \\ 0 & g_{22} & 0 \\ 0 & 0 & g_{33} \end{pmatrix},$$

with the associated reference frame $\langle \mathbf{N}, \mathbf{t}_1, \mathbf{t}_2 \rangle$, where $\mathbf{t}_1, \mathbf{t}_2$ span the tangent plane, while \mathbf{N} is the vector normal to the surface and is used to extend the tangent set to a basis of \mathbb{R}^3 . Then (1) can be re-written in divergence form as (see appendix Appendix A):

$$\nabla_{\mathbb{G}} \cdot \underline{\underline{F}} = -\mathbf{S}, \quad (2)$$

where $\nabla_{\mathbb{G}} \cdot$ is the intrinsic divergence with respect to the extended metric \mathbb{G} , and $\underline{\underline{F}}$ is an extended (symmetric) flux function defined as:

$$\underline{\underline{F}}(t, \mathbf{s}, \mathbf{U}) = \begin{bmatrix} \eta & q^1 & q^2 \\ q^1 & \frac{(q^1)^2}{\eta} + \frac{g\eta^2}{2h_{(1)}^2} \frac{\partial x^3}{\partial s^3} & \frac{q^1 q^2}{\eta} \\ q^2 & \frac{q^1 q^2}{\eta} & \frac{(q^2)^2}{\eta} + \frac{g\eta^2}{2h_{(2)}^2} \frac{\partial x^3}{\partial s^3} \end{bmatrix} = \begin{bmatrix} \eta & q^1 & q^2 \\ q^1 & F^{21} & F^{22} \\ q^2 & F^{31} & F^{32} \end{bmatrix}. \quad (3)$$

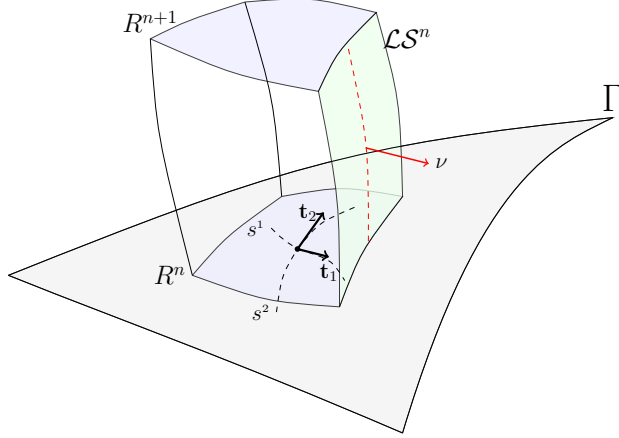


Figure 1: Illustration of the control volume D^n in the time-space intrinsic local coordinates, with $\partial D^n = R^n \cup \mathcal{L}S^n \cup \bar{R}^{n+1}$, where R^n is the inflow region, \bar{R}^{n+1} the outflow region and $\mathcal{L}S^n$ the no-flow surface.

2.2. The Intrinsic Lagrangian-Eulerian Scheme

We now turn our attention to the discretization of the ISWE system (2) and develop our extension of the scalar multidimensional Lagrangian-Eulerian method, introduced in [31], to the ISWE system written in covariant form. As standard in a finite volume framework, we work in the extended time-space domain consider a *Discrete Control Volume* in the Lagrangian-Eulerian local coordinate system defined by the region $D^n := [t^n, t^{n+1}] \times R \subset \mathbb{R} \times \Gamma$. We will be interested in applying the divergence theorem in this framework, and thus we need to properly define the boundary of this control volume. In particular, with reference to Figure 1, $\partial D = R^n \cup \mathcal{L}S^n \cup \bar{R}^{n+1}$ is the boundary of the control volume D formed by R^n and \bar{R}^{n+1} , the *Discrete Entry* and *Discrete Exit* of the flux at times t^n and t^{n+1} , and the lateral surface $\mathcal{L}S^n$, called *Discrete no-flow surface*. Testing equation (2) using the characteristic function of this discrete control volume we obtain:

$$\int_{D^n} \nabla_{\mathbb{G}} \cdot \underline{\underline{F}} = - \int_{D^n} \mathbf{S}.$$

Applying the divergence theorem yields:

$$\int_{\partial D^n} \langle \underline{\underline{F}}, \vec{n} \rangle_{\mathbb{G}} = - \int_{D^n} \mathbf{S} =: I(\mathbf{S}), \quad (4)$$

where $\langle \underline{\underline{F}}, \vec{n} \rangle_{\mathbb{G}} = \left\{ \underline{\underline{F}}^\beta \mathbb{G} \vec{n} \right\}^\beta$, $\beta = 1, 2, 3$, with $\underline{\underline{F}}^\beta$ the β -th row of the flux function (3). The vector \vec{n} denotes outward normal to the boundary ∂D (see central panel in Figure 1). It corresponds to the vector normal to the surface with $-$ sign in the entry region R^n , i.e. $-\mathbf{N}$, and analogously but with the opposite sign for the normal to the region \bar{R}^{n+1} . Note that, the vector \mathbf{N} is equal to $[1, 0, 0]^T$, when written in the time-space local coordinate system. As a consequence, the left-hand-side of equation (4) can be written as:

$$\begin{aligned} & \int_{R^n} \left\langle \underline{\underline{F}}, \begin{bmatrix} -1 \\ 0 \\ 0 \end{bmatrix} \right\rangle_{\mathbb{G}} + \int_{\mathcal{L}S^n} \langle \underline{\underline{F}}, \nu \rangle_{\mathbb{G}} + \int_{\bar{R}^{n+1}} \left\langle \underline{\underline{F}}, \begin{bmatrix} 1 \\ 0 \\ 0 \end{bmatrix} \right\rangle_{\mathbb{G}} = I(\mathbf{S}), \\ & - \int_{R^n} \mathbf{U}(t^n, s^1, s^2) + \int_{\mathcal{L}S^n} \langle \underline{\underline{F}}, \nu \rangle_{\mathbb{G}} + \int_{\bar{R}^{n+1}} \mathbf{U}(t^{n+1}, s^1, s^2) = I(\mathbf{S}), \end{aligned}$$

where ν is the normal to \mathcal{LS}^n written in the LCS (at each corresponding time t).

By virtue of the conceptual philosophy of the Lagrangian-Eulerian approach (see, e.g., [41, 31, 32]), we suppose that there is no-flow through the lateral surface \mathcal{LS}^n , and thus we impose the no-flow condition:

$$\int_{\mathcal{LS}^n} \langle \underline{\mathbf{F}}, \nu \rangle_{\mathbf{g}} = 0. \quad (5)$$

Hence, the evolution relation for the state variable is given by:

$$\int_{\bar{R}^{n+1}} \mathbf{U}(t^{n+1}, s^1, s^2) = \int_{R^n} \mathbf{U}(t^n, s^1, s^2) + I(\mathbf{S}). \quad (6)$$

Lagrangian-Eulerian model. With respect to the underlying geometrically intrinsic Lagrangian-Eulerian approach, the following two problems are equivalent in the weak (distributional) sense:

$$\text{(I)} \left\{ \begin{array}{l} \frac{\partial \mathbf{U}}{\partial t} + \nabla_{\mathbf{g}} \cdot \mathbf{F}(\mathbf{s}, \mathbf{U}) + \mathbf{S}(\mathbf{s}, \mathbf{U}) = 0 \\ \mathbf{U}(0, s^1, s^2) = \mathbf{U}_0 \end{array} \right.$$

and

$$\text{(II)} \left\{ \begin{array}{l} \int_{\mathcal{LS}^n} \langle \underline{\mathbf{F}}, \nu \rangle_{\mathbf{g}} = 0 \\ \frac{1}{A(R^{n+1})} \int_{\bar{R}^{n+1}} \mathbf{U}(t^{n+1}, s^1, s^2) = \frac{1}{A(R^{n+1})} \int_{R^n} \mathbf{U}(t^n, s^1, s^2) + \frac{1}{A(R^{n+1})} \int_{D^n} \mathbf{S} \\ \mathbf{U}(0, s^1, s^2) = \mathbf{U}_0, \end{array} \right.$$

where $A(\bar{R}^{n+1})$ denotes the area of the evolved region \bar{R}^{n+1} . Problem **(II)** represents the geometrically intrinsic Lagrangian-Eulerian building block, which will form the basis for our numerical scheme. Recalling that the regions R^n , \bar{R}^{n+1} and \mathcal{LS}^n are defined in a time-space reference frame, we can understand the Cauchy problem **(II)** to represent the Lagrangian evolution step followed by the projection onto the original region R^n obtained by imposing in an Eulerian sense the local mass conservation (Eulerian projection step).

2.2.1. Time-space discretization

We assume we are given a surface triangulation $\mathcal{T}(\Gamma)$ of the bottom surface Γ , fixed in time, formed by the union of non-intersecting geodesic triangles with vertices on Γ (edges are geodesics), and such that $\mathcal{T}(\Gamma) = \cup_{\ell=1}^{N_K} K_\ell = \bar{\Gamma}$ and $e_{\ell m} = K_\ell \cap K_m$ is an internal geodesic edge. The triangulation is characterized by a mesh parameter $h = \max_{\ell} \text{diam}(K_\ell)$. Together with the space discretization, we consider a time discretization $\{t^n\}$ of the time interval $[0, t_f]$, where we define a non-uniform time-step $\Delta t = t^{n+1} - t^n$. At each time t^n , the cell K_ℓ coincides with the inflow region R_ℓ^n , namely the triangulation $\mathcal{T}(\Gamma)$ is our working grid. We assume that each point of K_ℓ can be expressed in the tangent plane $T_{\mathbf{m}_\ell} \Gamma$ passing through the curved-cell mid-point \mathbf{m}_ℓ with an error of $\mathcal{O}(h^2)$, or more precisely, the distance between every point of K_i and its projection on $T_{\mathbf{m}_\ell} \Gamma$ is proportional to h^2 . This enables us to work on the flat cell defined by projecting the vertices of the curved cell on $T_{\mathbf{m}_\ell} \Gamma$.

We can define in each cell R_ℓ^n the approximate solution by:

$$\mathbf{U}_\ell^n := \frac{1}{A(R_\ell^n)} \int_{R_\ell^n} \mathbf{U}(t^n, s^1, s^2),$$

while, the approximate solution at time t^{n+1} , i.e., the mean value \mathbf{U}_ℓ^{n+1} over the region \bar{R}_ℓ^{n+1} , is obtained after a projection procedure (Eulerian projection step) over the original grid $K_\ell = R_\ell^n$ in the corresponding control volume. Denoting by $\bar{\mathbf{U}}_\ell^{n+1}$ the approximate value at time t^{n+1} obtained from the Lagrangian step

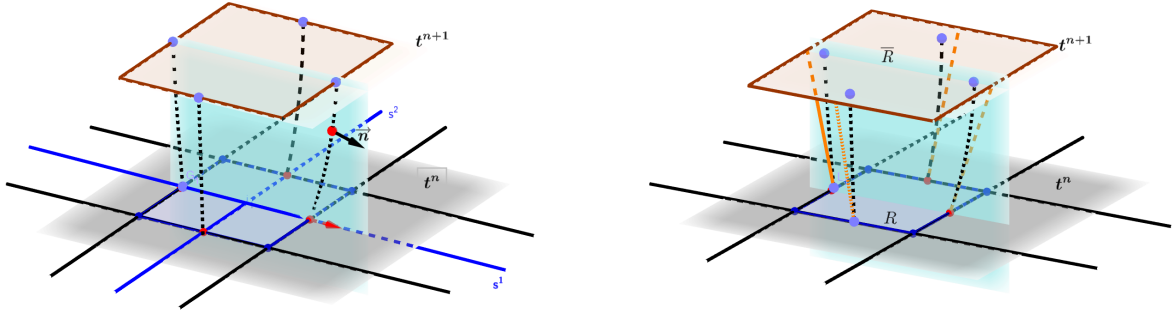


Figure 2: Approximation of the no-flow surface.

(6) along with the desired conservation properties, we can write:

$$\begin{aligned} \bar{\mathbf{U}}_\ell^{n+1} &= \frac{1}{A(\bar{R}_\ell^{n+1})} \int_{\bar{R}_\ell^{n+1}} \mathbf{U}(t^{n+1}, \mathbf{s}) \\ &= \frac{A(R_\ell^n)}{A(\bar{R}_\ell^{n+1})} \left[\frac{1}{A(R_\ell^n)} \int_{R_\ell^n} \mathbf{U}(t^n, \mathbf{s}) + \frac{1}{A(R_\ell^n)} I(\mathbf{S}) \right] = \frac{A(R_\ell^n)}{A(\bar{R}_\ell^{n+1})} \left[\mathbf{U}_\ell^n + \frac{1}{A(R_\ell^n)} I(\mathbf{S}) \right]. \end{aligned} \quad (7)$$

Approximation of the no-flow condition (5). In this paragraph we describe how to approximate equation (5) on each face $\mathcal{LS}_{\ell m}^n$ forming the lateral no-flow surface \mathcal{LS}_ℓ^n . For any time $\tau \in [t^n, t^{n+1}]$, the equation can be re-written separating space and time as:

$$0 = \int_{t^n}^\tau \int_{e_{\ell m}(t)} \langle \underline{F}(t, \mathbf{s}), \nu(t, \mathbf{s}) \rangle_{\mathbb{G}} \, ds \, dt \approx \int_{t^n}^\tau |e_{\ell m}|(t) \langle \underline{F}(t, \mathbf{m}_e), \nu(t, \mathbf{m}_e) \rangle_{\mathbb{G}} \, dt,$$

where $|e_{\ell m}|$ and \mathbf{m}_e are the length and the mid-point of $e_{\ell m}(t)$, respectively. Note that we used the mid-point rule for the space integral suggesting that the consistent characterization of the no-flow surface can be obtained by imposing:

$$\langle \underline{F}(t, \mathbf{m}_e), \nu(t, \mathbf{m}_e) \rangle_{\mathbb{G}} = \mathbf{0} \quad \forall t \in [t^n, t^{n+1}],$$

Now, we can identify the no-flow curve $\sigma_{\ell m} \subset \mathcal{LS}_{\ell m}^n$ that starts from \mathbf{m}_e and write its parametrization as (see figure 2, left):

$$\sigma_{\ell m}(t) = [t, \sigma_{\ell m}^1(t), \sigma_{\ell m}^2(t)].$$

The normal $\nu_{\ell m}(t) = \nu(t, \mathbf{m}_e)$ can be written implicitly in terms of $\sigma_{\ell m}'(t)$ in the time-space local reference system. This yields a nonlinear system of ODEs that describes $\sigma_{\ell m}'$ as a function of the SWE flux, with initial conditions given by $\sigma_{\ell m}(t^n) = [t^n, \mathbf{m}_e^1(t^n), \mathbf{m}_e^2(t^n)]^T$ and $\langle \nu_{\ell m}(t^n), \sigma_{\ell m}'(t^n) \rangle_{\mathbb{G}} = 0$. The system simplifies considerably if we linearize the equation around t^n , which is equivalent to apply explicit Euler to solve the above ODE (see figure 2, right). Following this approach, the position of the evolved mid-point at $t \in [t^n, t^{n+1}]$ can be calculated as:

$$\sigma_{\ell m}(t) = \sigma_{\ell m}(t^n) + (t - t^n) \sigma_{\ell m}'(t^n).$$

For example, in the case of an edge with the unit tangent vector in $\mathbf{m}_e(t^n)$ that is aligned with \mathbf{t}_2 , we obtain explicitly $\sigma_{\ell m}' = [1, (\sigma_{\ell m}^1)']^T$ by solving the following linear system:

$$0 = \langle \underline{F}(t^n, \mathbf{m}_e), \nu(t^n, \mathbf{m}_e) \rangle_{\mathbb{G}} \Big|^\beta = \underline{F}^\beta(t^n, \mathbf{m}_e) \mathbb{G}(\mathbf{m}_e) \begin{bmatrix} -1 \\ 1 \\ \frac{(\sigma_{\ell m}^{1\beta})'(t^n)}{0} \end{bmatrix}, \quad (8)$$

for each component $\beta = 1, 2, 3$.

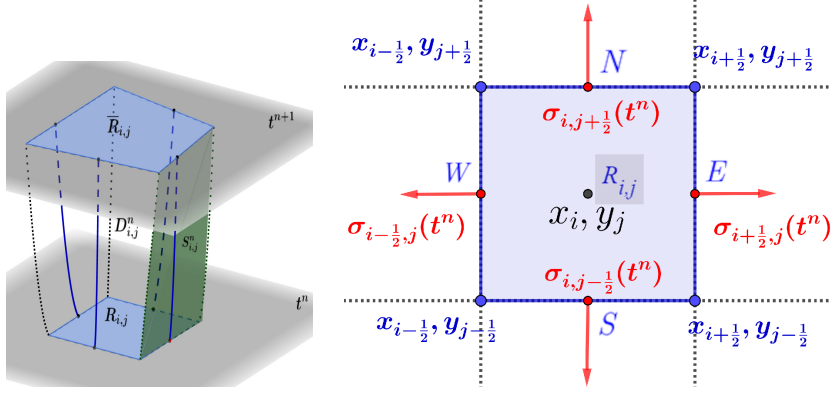


Figure 3: Notation in the Cartesian case. No-flow curves $\sigma_{i-\frac{1}{2},j}(t)$, $\sigma_{i+\frac{1}{2},j}(t)$, $\sigma_{i,j-\frac{1}{2}}(t)$ and $\sigma_{i,j+\frac{1}{2}}(t)$ for each edge.

Discrete Lagrangian-Eulerian scheme. We can summarize the fully discrete version of problem **(II)** forming our proposed Lagrangian-Eulerian finite volume scheme as follows:

$$\left\{ \begin{array}{l} \sigma_{\ell m}(t^{n+1}) = \sigma_{\ell m}(t^n) + \Delta t \sigma'_{\ell m}(t^n), \quad \text{where} \\ \langle \nu_{\ell m}(t^n), \sigma'_{\ell m}(t^n) \rangle_{\mathbb{G}} = 0 \quad \text{and} \quad \langle \underline{F}(t^n, \mathbf{m}_e), \nu(t^n, \mathbf{m}_e) \rangle_{\mathbb{G}} = \mathbf{0} \quad \text{and} \quad \sigma_{e_{\ell m}}(t^n) = [t^n, \mathbf{m}_e^1, \mathbf{m}_e^2]^{\top} \\ \bar{\mathbf{U}}_{\ell}^{n+1} = \frac{A(R_{\ell}^n)}{A(\bar{R}_{\ell}^{n+1})} \left[\mathbf{U}_{\ell}^n + \frac{1}{A(R_{\ell}^n)} \int_{R_{\ell}^n} \mathbf{S} \right], \\ \mathbf{U}_{\ell}(0, \mathbf{m}_{\ell}^1, \mathbf{m}_{\ell}^2) = \mathbf{U}_0. \end{array} \right.$$

The numerical formulation is completed by the Eulerian projection step, which, depending on the geometry of the cells, is described in the next section. The approach is simple and robust in terms of accuracy and computational cost, since simple quadrature formulae as such trapezoidal and midpoint rules can be employed for the approximation of the source term \mathbf{S} (see, e.g., [27, 28, 32, 42]).

3. Special case: Cartesian grid

In this section, we consider a special tringulation $\mathcal{T}(\Gamma)$ of Γ defined from a regular square Cartesian grid of the \mathbb{R}^2 chart by vertical projection of the vertices onto the surface. Thus, we can use local flat coordinates defined on $T_{\mathbf{m}_e} \Gamma$ for each cell K_{ℓ} . We will denote by (x, y) the local flat coordinates. We use the lattice $\mathbb{N} \times (\mathbb{Z} \times \mathbb{Z}) = \{(n, i, j) : n = 0, 1, 2, \dots, i, j = 0, \pm 1, \pm 2, \dots\}$ to describe the Cartesian grid of the chart for each time t^n . We denote by $h_x^n = \Delta x^n = x_{i+\frac{1}{2}}^n - x_{i-\frac{1}{2}}^n$, and $h_y^n = \Delta y^n = y_{j+\frac{1}{2}}^n - y_{j-\frac{1}{2}}^n$, where $(x_{i\pm\frac{1}{2}}^n, y_{j\pm\frac{1}{2}}^n)$ are the corners of the (i, j) -cell defined on $T_{\mathbf{m}_i} \Gamma$. The cell centers and vertices are then given by:

$$(x_i^n, y_j^n) = (ih_x^n, jh_y^n) \quad \text{and} \quad (x_{i\pm\frac{1}{2}}^n, y_{j\pm\frac{1}{2}}^n) = \left(ih_x^n \pm \frac{h_x^n}{2}, jh_y^n \pm \frac{h_y^n}{2} \right).$$

The Lagrangian-Eulerian control volume $D_{i,j}^n$ (figure 3) is the volume comprised by the union of the surface $\partial D_{i,j}^n = R_{i,j}^n \cup \mathcal{L}S_{i,j}^n \cup \bar{R}_{i,j}^{n+1}$ described in the LCS mesh grid by:

- $R_{i,j}^n = [x_{i-\frac{1}{2}}^n, x_{i+\frac{1}{2}}^n] \times [y_{j-\frac{1}{2}}^n, y_{j+\frac{1}{2}}^n]$ the inflow of $\partial D_{i,j}^n$;
- $\bar{R}_{i,j}^{n+1} = [\bar{x}_{i-\frac{1}{2}}^{n+1}, \bar{x}_{i+\frac{1}{2}}^{n+1}] \times [\bar{y}_{j-\frac{1}{2}}^{n+1}, \bar{y}_{j+\frac{1}{2}}^{n+1}]$ the outflow of $\partial D_{i,j}^n$;

- $\mathcal{LS}_{i,j}^n$, the lateral no-flow surface, formed by North (N), East (E), South (S), and West (W) edges as indicated in figure 3.

The area of every computational square cell $\left[x_{i-\frac{1}{2}}^n, x_{i+\frac{1}{2}}^n\right] \times \left[y_{j-\frac{1}{2}}^n, y_{j+\frac{1}{2}}^n\right]$ (see figure 3, right) is $A(R_{i,j}^n) = h_x^n h_y^n$, so that the approximate solution is:

$$\mathbf{U}_{i,j}^n = \frac{1}{A(R_{i,j}^n)} \int_{x_{i-\frac{1}{2}}^n}^{x_{i+\frac{1}{2}}^n} \int_{y_{j-\frac{1}{2}}^n}^{y_{j+\frac{1}{2}}^n} \mathbf{U}(t^n, x, y) dx dy,$$

with analogous expression for the average solution $\bar{\mathbf{U}}(t^{n+1}, x_i, y_j)$ in the evolved region \bar{R}^{n+1} . We recall that the approximate solution $\mathbf{U}_{i,j}^{n+1}$ at time t^{n+1} is obtained after the projection procedure (Eulerian projection step) over the original grid (see figure 3, left). Using this notation, equation (7) provides the expression of our finite volume scheme in this Cartesian setting.

Approximation of the no-flow surfaces $\mathcal{LS}_{i,j}^n$. The approximation of the integrals on the no-flow surfaces follows the procedure described in section 2.2.1. For instance, the parametrization of the no-flow curve for the edge N is indicated by $\sigma_N(t) = \sigma_{i,j+\frac{1}{2}}(t) = [t, \sigma_N^1(t), \sigma_N^2(t)]$, and the normal vector at t^n is given by $\nu = \left[-1, 0, \frac{1}{(\sigma_N^{2\beta})'(t^n)}\right]^T$. Then, equation (8) becomes:

$$0 = \langle \underline{F}, \nu \rangle_{\mathbb{G}} \Big|_{\mathbb{G}}^{\beta} = \underline{F}^{\beta} \mathbb{G} \begin{bmatrix} -1 \\ 0 \\ 1 \\ \frac{1}{(\sigma_N^{2\beta})'(t^n)} \end{bmatrix},$$

resulting in:

$$(\sigma_N^{2\beta})'(t^n) = \underline{F}^{(\beta,3)} h_{(2)}^2 / \mathbf{U}^{\beta,n}, \quad \beta = 1, 2, 3.$$

On the other hand, for edge W , the normal vector at t^n is given by $\nu = \left[-1, \frac{1}{(\sigma_W^{2\beta})'(t^n)}, 0\right]^T$, and equation (8) reads:

$$0 = \langle \underline{F}, \nu \rangle_{\mathbb{G}} \Big|_{\mathbb{G}}^{\beta} = \underline{F}^{\beta} \mathbb{G} \begin{bmatrix} -1 \\ 1 \\ \frac{1}{(\sigma_W^{1\beta})'(t^n)} \\ 0 \end{bmatrix},$$

thus:

$$(\sigma_W^{1\beta})'(t^n) = \underline{F}^{(\beta,2)} h_{(1)}^2 / \mathbf{U}^{\beta,n}, \quad \beta = 1, 2, 3.$$

In summary, we have the following four expressions for each equation of the discrete ISWE system for $\beta = 1, 2, 3$ associated to each sides N, E, S and W , respectively:

$$(\sigma_N^{2\beta})'(t^n) = \frac{\underline{F}^{(\beta,3)} h_{(2)}^2}{\mathbf{U}^{\beta,n}}, \quad (\sigma_E^{1\beta})'(t) = \frac{\underline{F}^{(\beta,2)} h_{(1)}^2}{\mathbf{U}^{\beta,n}}, \quad (\sigma_S^{2\beta})'(t) = \frac{\underline{F}^{(\beta,3)} h_{(2)}^2}{\mathbf{U}^{\beta,n}}, \quad (\sigma_W^{1\beta})'(t) = \frac{\underline{F}^{(\beta,2)} h_{(1)}^2}{\mathbf{U}^{\beta,n}}.$$

Finally, for each edge, the linearization in time reads as follows:

$$\sigma_{i-\frac{1}{2},j}^{\beta}(t) \approx x_{i-\frac{1}{2}} + (t - t^n) \frac{\underline{F}^{(\beta,2)} h_{(1)}^2}{\mathbf{U}^{\beta,n}} \quad \text{and} \quad \sigma_{i+\frac{1}{2},j}^{\beta}(t) \approx x_{i+\frac{1}{2}} + (t - t^n) \frac{\underline{F}^{(\beta,2)} h_{(1)}^2}{\mathbf{U}^{\beta,n}}, \quad (9)$$

$$\sigma_{i,j-\frac{1}{2}}^{\beta}(t) \approx y_{j-\frac{1}{2}} + (t - t^n) \frac{\underline{F}^{(\beta,3)} h_{(2)}^2}{\mathbf{U}^{\beta,n}} \quad \text{and} \quad \sigma_{i,j+\frac{1}{2}}^{\beta}(t) \approx y_{j+\frac{1}{2}} + (t - t^n) \frac{\underline{F}^{(\beta,3)} h_{(2)}^2}{\mathbf{U}^{\beta,n}}, \quad (10)$$

for $t^n < t \leq t^{n+1}$.

The geometrically intrinsic Lagrangian-Eulerian building block on a regular Cartesian grid is summarized as follows:

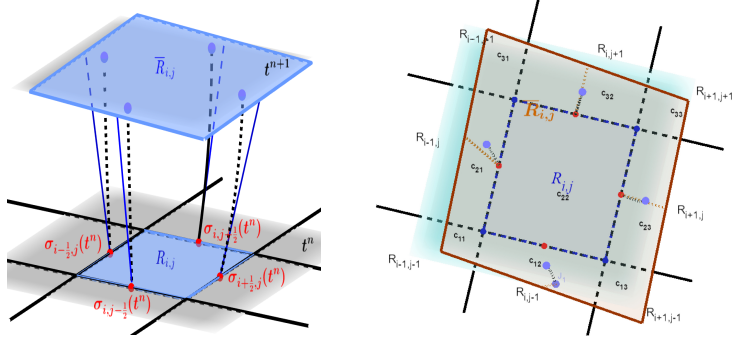


Figure 4: Summary of the Geometrically Intrinsic Lagrangian-Eulerian construction in the Cartesian case.

• **STEP I** (Lagrangian evolution step)

$$\left\{ \begin{array}{l} \sigma_{i\pm\frac{1}{2},j}^\beta(t^{n+1}) = x_{i\pm\frac{1}{2}} + \Delta t \frac{\underline{F}_{E/W}^{(\beta,2)} h_{(1)}^2}{\mathbf{U}^{\beta,n}} \quad \text{and} \quad \sigma_{i,j\pm\frac{1}{2}}^\beta(t^{n+1}) = y_{j\pm\frac{1}{2}} + \Delta t \frac{\underline{F}_{N/S}^{(\beta,3)} h_{(2)}^2}{\mathbf{U}^{\beta,n}} \\ \bar{\mathbf{U}}_{i,j}^{n+1} = \frac{A(R_{i,j}^n)}{A(\bar{R}_{i,j}^{n+1})} \left[\mathbf{U}_{i,j}^n + \frac{1}{A(R_{i,j}^n)} \int_{R_{i,j}^n} \mathbf{S}^\beta \right] \\ \mathbf{U}_{i,j}^\beta(0) = \mathbf{U}_0^\beta \end{array} \right. \quad (11)$$

for all equations $\beta = 1, 2, 3$, with

$$A(\bar{R}_{i,j}^{n+1}) = \left[h_x^n - \left(\frac{\underline{F}_{E}^{(\beta,2)} h_{(1)}^2}{\mathbf{U}^{\beta,n}} - \frac{\underline{F}_{W}^{(\beta,2)} h_{(1)}^2}{\mathbf{U}^{\beta,n}} \right) \Delta t \right] \left[h_y^n - \left(\frac{\underline{F}_{N}^{(\beta,3)} h_{(2)}^2}{\mathbf{U}^{\beta,n}} - \frac{\underline{F}_{S}^{(\beta,3)} h_{(2)}^2}{\mathbf{U}^{\beta,n}} \right) \Delta t \right].$$

• **STEP II** (Eulerian projection step)

$$\mathbf{U}_{i,j}^{n+1} = \frac{1}{A(\bar{R}_{i,j}^{n+1})} (C1 + C2 + C3), \quad (12)$$

with

$$C1 = c_{11} \bar{\mathbf{U}}_{i-1,j-1}^{n+1} + c_{12} \bar{\mathbf{U}}_{i,j-1}^{n+1} + c_{13} \bar{\mathbf{U}}_{i+1,j-1}^{n+1}, \quad C2 = c_{21} \bar{\mathbf{U}}_{i-1,j}^{n+1} + c_{22} \bar{\mathbf{U}}_{i,j}^{n+1} + c_{23} \bar{\mathbf{U}}_{i+1,j}^{n+1},$$

$$C3 = c_{31} \bar{\mathbf{U}}_{i-1,j+1}^{n+1} + c_{32} \bar{\mathbf{U}}_{i,j+1}^{n+1} + c_{33} \bar{\mathbf{U}}_{i+1,j+1}^{n+1},$$

where the coefficients c_{ij} are defined as the entries of the matrix (see figure 4)

$$C = (c_{ij}) = C_x^T C_y, \quad i, j \in \{1, 2, 3\},$$

under the CFL-condition:

$$\max_{i,j,\beta} \left\{ \left| \frac{\underline{F}_{N}^{(\beta,3)} h_{(2)}^2}{\mathbf{U}^{\beta,n}} \right|, \left| \frac{\underline{F}_{E}^{(\beta,2)} h_{(1)}^2}{\mathbf{U}^{\beta,n}} \right|, \left| \frac{\underline{F}_{S}^{(\beta,3)} h_{(2)}^2}{\mathbf{U}^{\beta,n}} \right|, \left| \frac{\underline{F}_{W}^{(\beta,2)} h_{(1)}^2}{\mathbf{U}^{\beta,n}} \right| \right\} \frac{\Delta t}{h} < \frac{1}{2}, \quad (13)$$

and the assumption $h = \Delta x = \Delta y$. The expression for C_x and C_y takes on the form:

$$C_x = [C_{xl}, \Delta x - C_{xl} - C_{xr}, C_{xr}], \quad \text{and} \quad C_y = [C_{yr}, \Delta y - C_{yr} - C_{yl}, C_{yl}], \quad (14)$$

assuming:

$$C_{xl} = 0.5 \left[1 + \text{sign} \left(\frac{F^{(\beta,2)} h_{(1)}^2}{\mathbf{U}^{\beta,n}} \right) \right] \frac{F^{(\beta,2)} h_{(1)}^2}{\mathbf{U}^{\beta,n}} \Delta t, \quad C_{xr} = 0.5 \left[1 - \text{sign} \left(\frac{F^{(\beta,2)} h_{(1)}^2}{\mathbf{U}^{\beta,n}} \right) \right] \frac{F^{(\beta,2)} h_{(1)}^2}{\mathbf{U}^{\beta,n}} \Delta t,$$

$$C_{yl} = 0.5 \left[1 + \text{sign} \left(\frac{F^{(\beta,3)} h_{(2)}^2}{\mathbf{U}^{\beta,n}} \right) \right] \frac{F^{(\beta,3)} h_{(2)}^2}{\mathbf{U}^{\beta,n}} \Delta t, \quad C_{yr} = 0.5 \left[1 - \text{sign} \left(\frac{F^{(\beta,3)} h_{(2)}^2}{\mathbf{U}^{\beta,n}} \right) \right] \frac{F^{(\beta,3)} h_{(2)}^2}{\mathbf{U}^{\beta,n}} \Delta t.$$

3.1. Improved spatial resolution of the fully-discrete Lagrangian-Eulerian scheme

Improved spatial resolution can be obtained by means of a linear reconstruction of the quantities $\mathbf{U}_{i,j}^n$ in (11) and $\mathbf{U}_{i,j}^{n+1}$ in (12), which translates in a better approximation of the discrete no-flow surfaces. Following [43, 31, 33], the piecewise constant numerical data is reconstructed into a piecewise linear approximation through the use of MUSCL-type interpolants: $\mathbf{L}_{i,j}(t, x) = \mathbf{U}_{i,j}(t) + (x - x_j) \mathbf{U}'_{i,j}/h$, in the x -direction. The interpolation in the y -direction is similar. For the numerical derivative $\mathbf{U}'_{i,j}/h$, there are several choices of slope limiters for scalar case, and [44] contains a good compilation of possible options. Let us consider the parametric no-flow curve $\sigma_{i-\frac{1}{2},j}(t)$, the other cases are similar. A straightforward calculation leads to:

$$\mathbf{U}_{i-\frac{1}{2},j} = \frac{1}{h} \left[\int_{x_{i-1,j}^n}^{x_{i-\frac{1}{2},j}^n} \mathbf{L}_{i-1,j}(t, x) dx + \int_{x_{i-\frac{1}{2},j}^n}^{x_{i,j}^n} \mathbf{L}_{i,j}(t, x) dx \right] = \frac{1}{2} (\mathbf{U}_{i-1,j} + \mathbf{U}_{i,j}) + \frac{1}{8} (\mathbf{U}'_{i,j} - \mathbf{U}'_{i-1,j}). \quad (15)$$

Finally, in order to show the flexibility of the reconstruction, we use the nonlinear Lagrange polynomial in $\mathbf{U}_{i-1,j}^n$, $\mathbf{U}_{i,j-1}^n$, $\mathbf{U}_{i,j}^n$, $\mathbf{U}_{i,j+1}^n$ and $\mathbf{U}_{i+1,j}^n$. Therefore, equation (11) reads:

$$\bar{\mathbf{U}}_{i,j}^{n+1} = \frac{1}{h} \int_{w_{j-\frac{1}{2}}}^{w_{j+\frac{1}{2}}} \mathbf{P}_2(x, y) dw, \quad \text{where } w = x, y$$

and

$$\mathbf{P}_2(x, y) = \mathbf{U}_{i-1,j}^n \mathbf{L}_{-1}(x - x_i) + \mathbf{U}_{i,j-1}^n \mathbf{L}_{-1}(y - y_j) \\ + \mathbf{U}_{i,j}^n \mathbf{L}_0(x - x_i) + \mathbf{U}_{i,j}^n \mathbf{L}_0(y - y_j) + \mathbf{U}_{i+1,j}^n \mathbf{L}_1(x - x_j) + \mathbf{U}_{i,j+1}^n \mathbf{L}_1(y - y_j),$$

with

$$\mathbf{L}_{\pm 1}(x) = \frac{1}{2} \left[\left(\frac{x}{h} \pm \frac{1}{2} \right)^2 - \frac{1}{4} \right], \quad \mathbf{L}_0(x) = 1 - \left(\frac{x}{h} \right)^2.$$

3.2. A connection with monotone finite difference (volume) schemes

The fact that each working cell is assumed to be a subset of the tangent plane $T_{m_\ell} \Gamma$ allows us to recast our proposed scheme within the framework of monotone finite difference schemes (see [45, 46, 47]). This theory is developed only for the case of scalar hyperbolic equations, thus in the following we consider $\frac{\partial U}{\partial t} + \nabla \cdot \mathbf{F}(U) = 0$, where $\mathbf{F}(U) = [\mathcal{F}_1, \mathcal{F}_2]$. Under the CFL stability constraint (13) and switching-off the linear reconstruction of the quantities $U_{i,j}^n, U_{i,j}^{n+1}$, the fully-discrete Lagrangian-Eulerian scheme (11)-(12) can be written as:

$$U_{i,j}^{n+1} = C_x A_{i,j}^T C_y^T, \quad A_{i,j} = \begin{bmatrix} \bar{U}_{i-1,j-1}^{n+1} & \bar{U}_{i,j-1}^{n+1} & \bar{U}_{i+1,j-1}^{n+1} \\ \bar{U}_{i-1,j}^{n+1} & \bar{U}_{i,j}^{n+1} & \bar{U}_{i+1,j}^{n+1} \\ \bar{U}_{i-1,j+1}^{n+1} & \bar{U}_{i,j+1}^{n+1} & \bar{U}_{i+1,j+1}^{n+1} \end{bmatrix},$$

or, in the classical form of conservative monotone scheme [31, 48], as:

$$U_{i,j}^{n+1} = U_{i,j}^n - \lambda^x \Delta_x^x F(U_{i-1,j-1}^n, \dots, U_{i+1,j+1}^n) - \lambda^y \Delta_y^y G(U_{i-1,j-1}^n, \dots, U_{i+1,j+1}^n), \quad (16)$$

Here, using the standard notations, we define $h = \Delta x = \Delta y$, and $\lambda^x = \Delta t / \Delta x$, $\lambda^y = \Delta t / \Delta y$, and $(\Delta_+^x U)_{j,k} = U_{j+1,k} - U_{j,k}$, $(\Delta_+^y U)_{j,k} = U_{j,k+1} - U_{j,k}$, and we can write:

$$F(U_{i-1,j-1}^n, \dots, U_{i+1,j+1}^n) = F_R(U_{i,j-1}^n, U_{i-1,j-1}^n, U_{i-1,j}^n, U_{i,j}^n, U_{i,j-1}^n) \\ - F_L(U_{i-1,j+1}^n, U_{i-1,j}^n, U_{i,j-1}^n, U_{i,j}^n, U_{i,j+1}^n),$$

with

$$F_R = h C_{xl} (\bar{U}_{i+1,j}^{n+1} - \bar{U}_{i,j}^{n+1}) \\ - C_{xl} C_{yr} (\bar{U}_{i-1,j+1}^{n+1} - \bar{U}_{i-1,j}^{n+1} - (\bar{U}_{i,j+1}^{n+1} - \bar{U}_{i,j}^{n+1})) + \frac{1}{2} (f(U_{i-1,j}^n) + 2f(U_{i,j}^n) + f(U_{i+1,j}^n)), \\ F_L = h C_{xl} (\bar{U}_{i-1,j}^{n+1} - \bar{U}_{i,j}^{n+1}) \\ - C_{xl} C_{yl} (\bar{U}_{i-1,j-1}^{n+1} - \bar{U}_{i,j-1}^{n+1} - (\bar{U}_{i-1,j}^{n+1} - \bar{U}_{i,j}^{n+1})) + \frac{1}{2} (f(U_{i-1,j}^n) + 2f(U_{i,j}^n) + f(U_{i+1,j}^n)),$$

and

$$G(U_{i-1,j-1}^n, \dots, U_{i+1,j+1}^n) = G_R(U_{i-1,j}^n, U_{i,j}^n, U_{i+1,j+1}^n, U_{i,j+1}^n, U_{i+1,j}^n) \\ - G_L(U_{i+1,j}^n, U_{i,j}^n, U_{i,j-1}^n, U_{i+1,j}^n, U_{i,j+1}^n),$$

with

$$G_R = h C_{yl} (\bar{U}_{i,j+1}^{n+1} - \bar{U}_{i,j}^{n+1}) \\ - C_{yl} C_{xr} (\bar{U}_{i+1,j-1}^{n+1} - \bar{U}_{i+1,j}^{n+1} - (\bar{U}_{i,j-1}^{n+1} - \bar{U}_{i,j}^{n+1})) + \frac{1}{2} (g(U_{i,j-1}^n) + 2g(U_{i,j}^n) + g(U_{i,j+1}^n)), \\ G_L = h C_{yl} (\bar{U}_{i,j-1}^{n+1} - \bar{U}_{i,j}^{n+1}) \\ - C_{yr} C_{xl} (\bar{U}_{i+1,j+1}^{n+1} - \bar{U}_{i+1,j}^{n+1} - (\bar{U}_{i,j+1}^{n+1} - \bar{U}_{i,j}^{n+1})) + \frac{1}{2} (g(U_{i,j-1}^n) + 2g(U_{i,j}^n) + g(U_{i,j+1}^n)).$$

In order for the scheme (16) be consistent for the 2D scalar case, we must have:

$$F(u, u, \dots, u) = \mathcal{F}_1(u) \quad \text{and} \quad G(u, u, \dots, u) = \mathcal{F}_2(u), \quad u \in \mathbb{R}. \quad (17)$$

We can notice that F and G satisfy condition (17). This implies consistency with $\frac{\partial U}{\partial t} + \nabla \cdot \mathbf{F}(U) = 0$. Indeed, it turns out that conservative monotone schemes as in (16) converge to entropy solutions [49, 48, 44]. It is possible to write the Lagrangian-Eulerian scheme applied to scalar equations in the form of standard monotone finite difference schemes (see, e.g., [42, 50, 31, 32, 33, 27, 29, 28, 30, 34]), showing that no Riemann problems are needed to obtain a correct entropy solution. Generalization to systems can be done only for special cases, and its identification for the ISWE system is subject of current studies.

4. Numerical simulations

The numerical experiments presented in this section are devised in order to show that the geometrically intrinsic Lagrangian-Eulerian scheme is able to handle non-autonomous fluxes coming from the spatial variability of the bottom topography and preserve the well-balance property of the system in the discrete setting. We define verify experimentally the applicability of the scheme on different surfaces by qualitatively comparing the numerical results against the benchmarks published in [2, 25]. In addition, we use for all the test cases long-time simulations to test the well-balance property of the proposed scheme by running the code until $t = 50$ s.

All the test cases consider a gravity-driven flow in a dam-break setting, with $T_{sw} = 0$ and $\tau_b = 0$, and no-flow boundary conditions. Initial condition is set to describe the dam-break, with zero velocity and depth

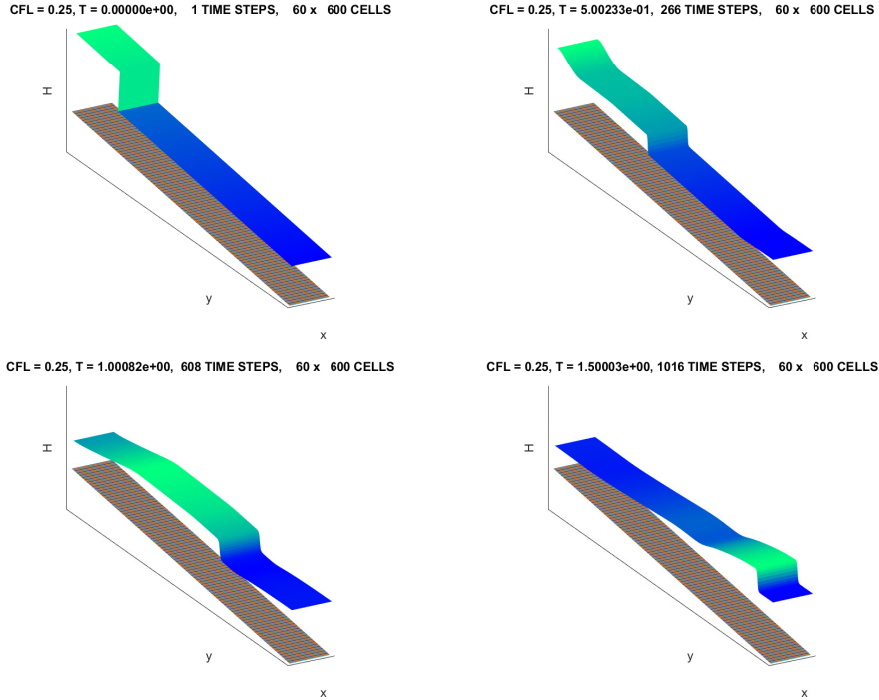


Figure 5: Sloping plane: evolution of the water depth at times $t=0, 0.5, 1, 1.5$ s.

defined differently on each surface, according to the specific geometry. Initial conditions will be specified for each test case. The CFL condition (13) is used to define an appropriate time-step size at every time step. Verification of the well-balance property is performed by looking at the time-behavior of the L_1 discrete norm:

$$\|\mathbf{S}\|_1 = A(R_{i,j}^n) \sum_{i,j} |\mathbf{S}_{i,j}|.$$

We consider four different bottom surfaces with an increasing complexity in the geometry: i) a simple sloping plane (i.e., constant metric), ii) a parabola (i.e., one-dimensional curvature effects), iii) a hyperboloid with a central bump (i.e., two-dimensional dependence of the geometry with a central radial symmetry), and iv) a fully three-dimensional surface. In all test cases we define our surface by the use of a global parametrization, where the height function is given in input as $x^3 = H(x, y)$. The working grid is obtained from a regular Cartesian grid of a subset $U \subset \mathbb{R}^2$ expressing the chart by moving the vertices of the squares vertically to the surface Γ .

Sloping plane. The chart domain is the rectangle $U = [0, 1] \times [0, 10] \subset \mathbb{R}^2$ and the height function is given by $H(x, y) = 0.1y + 1.0$. The initial value for the water depth is set to 2 m for cells located upstream of the dam position, located at $y = 2.0$ m, and a depth of 1 m downstream. A CFL value of 0.20 is considered to run the simulation.

Figure 5 shows the evolution of the normal depth at times $t = 0, 0.5, 1, 1.5$ s on a grid formed by 60×60 cells along the x and y -directions, respectively. Figures 6 and 7 show the water depth at $t = 1.5$ s and $t = 50$ s (top panels) over a mesh with 40×40 cells and 80×80 cells, respectively. The L^1 -norm of \mathbf{S} is plotted in the bottom panels. The results are very similar to those of [2, 25].

Parabola. In this test case we consider a simple one-dimensional flow in which the effect of the curvature is present. The parabola is defined by the height function $H(x, y) = 0.04(y - 10)^2$ on the rectangular domain

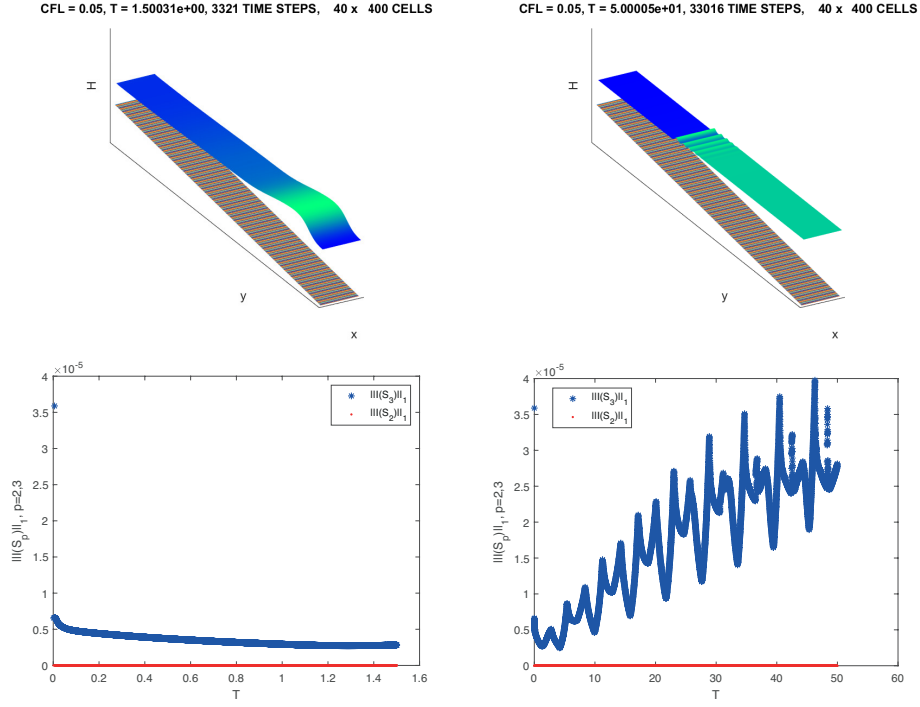


Figure 6: Sloping plane, 40×400 cells: water depth (top panels) and plots of the L^1 -norm of $I(\mathbf{S}^2)$ and $I(\mathbf{S}^3)$ (bottom panels), at times $t = 1.5$ s (left) and $t = 50$ s (right). Computational time for $t = 50$: 490.75 s.

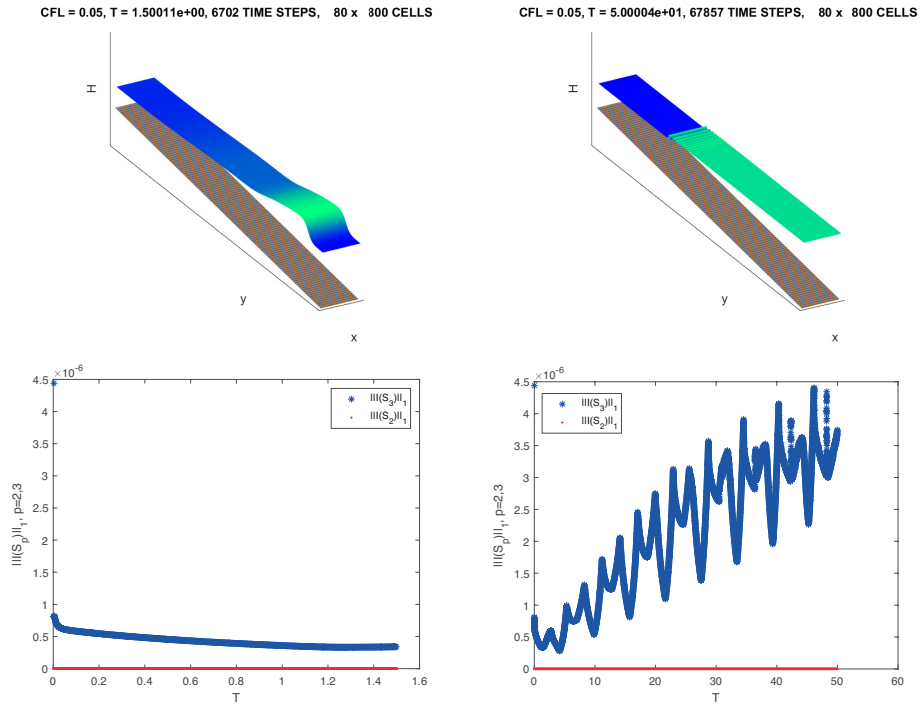


Figure 7: Sloping plane, 80×800 cells: water depth (top panels) and plots of the L^1 -norm of $I(\mathbf{S}^2)$ and $I(\mathbf{S}^3)$ (bottom panels) at time $t = 1.5$ s (left) and $t = 50$ s (right). Computational time for $t = 50$: 2726 s.

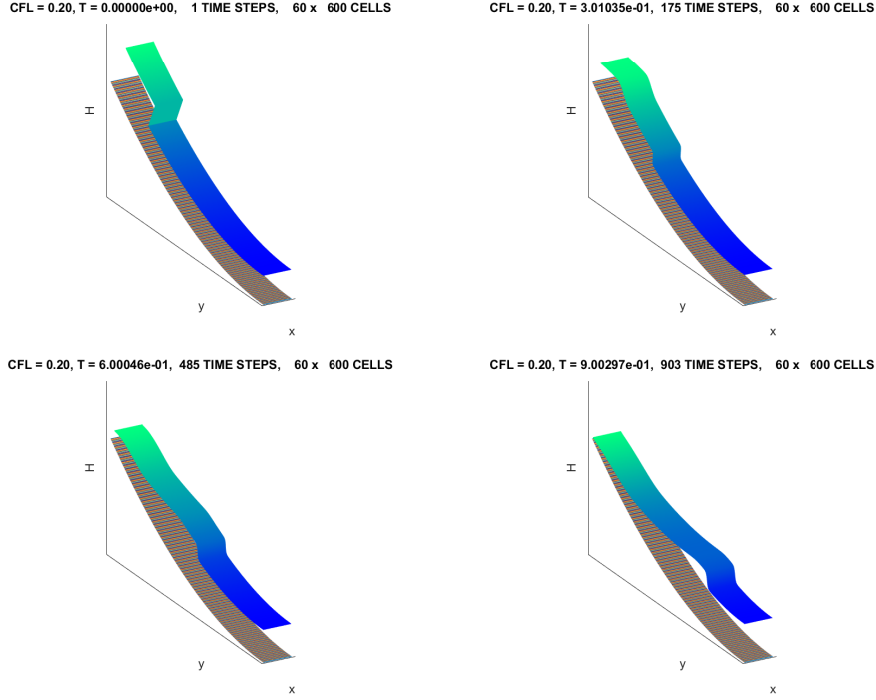


Figure 8: Parabola case: evolution of the water depth at times $t = 0.0, 0.3, 0.6, 0.9$ s.

$U = [0, 1] \times [0, 10] \subset \mathbb{R}^2$. The initial depth is 2 m of water upstream and 1 m downstream of the dam located at $y = 2.0$ m and a CFL value of 0.30 is considered.

Figure 8 shows the normal water depth evolution at times $t = 0.0, 0.30, 0.6, 0.9$ s on a grid formed by 60×60 cells. Figure 9 presents the numerical results to verify the discrete well-balanced property on a 40×40 grid. The long time well-balance error tends to decrease maintaining a maximum value below 10^{-4} at all times. The same simulation was run on a 80×80 grid with results consistent with the finer resolution.

Hyperboloid-central-bump. The third example considers a surface defined by the height function:

$$H(x, y) = -\frac{4}{5} \sqrt{(x)^2 + (y)^2 + 1}$$

on a two-dimensional square domain $U = [-3, 3] \times [-3, 3] \subset \mathbb{R}^2$. In this case the bottom surface presents curvatures in both directions. The initial condition is defined in order to capture the radial symmetric feature of the bottom surface in the behavior of the solution: 2 m of water are considered in the central part of the domain, i.e. inside of a circle of radius 0.5 m, and 1 m outside of this central radius. A CFL number of 0.30 is chosen in the condition (13).

The time evolution of the normal water depth at different times ($t = 0.0, 0.2, 0.4, 0.6$ s) is shown in figure 10 on a grid formed by 60×60 cells. Steady-state results are reported in figure 11 for a 40×40 cells grid. Again the results clearly show the effectiveness of the proposed scheme.

Fully 3D surface. The final surface is designed to highlight the behavior of the proposed scheme when positive and negative curvatures are present and to test its effectiveness in handling complex wetting and drying patterns. The height function is given by:

$$H(x, y) = -\frac{1}{500}(y)^3 - \frac{1}{100}y(x)^2$$

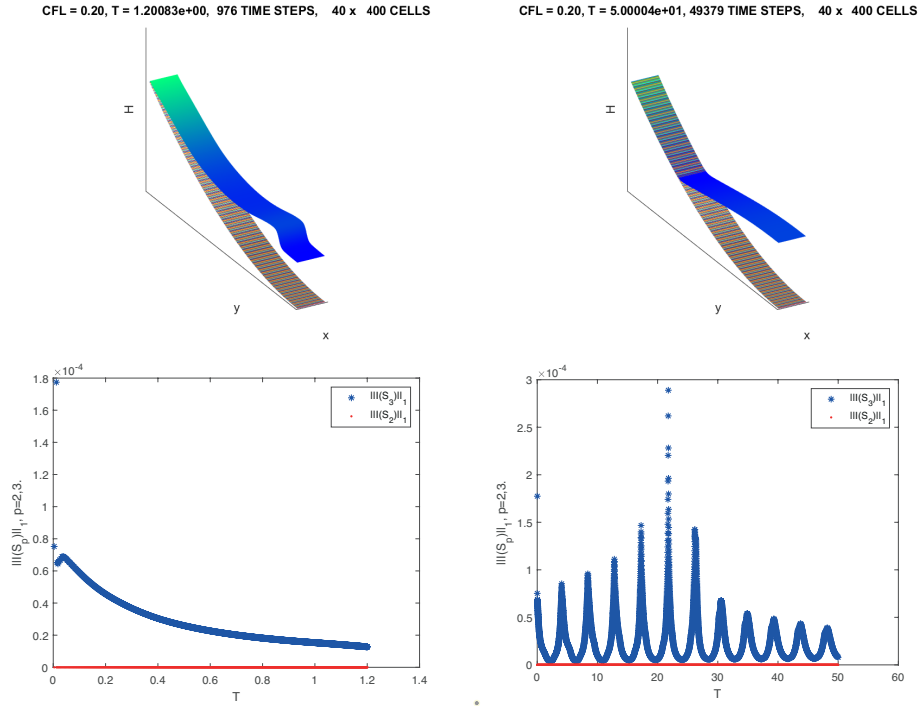


Figure 9: Parabola case, 40×400 cells: water depth (top panels) and plots of the L^1 -norm of $I(S^2)$ and $I(S^3)$ (bottom panels), at times $t = 1.2$ s (left) and $t = 50$ s (right). Computational time for $t = 50$: 676.11 s.

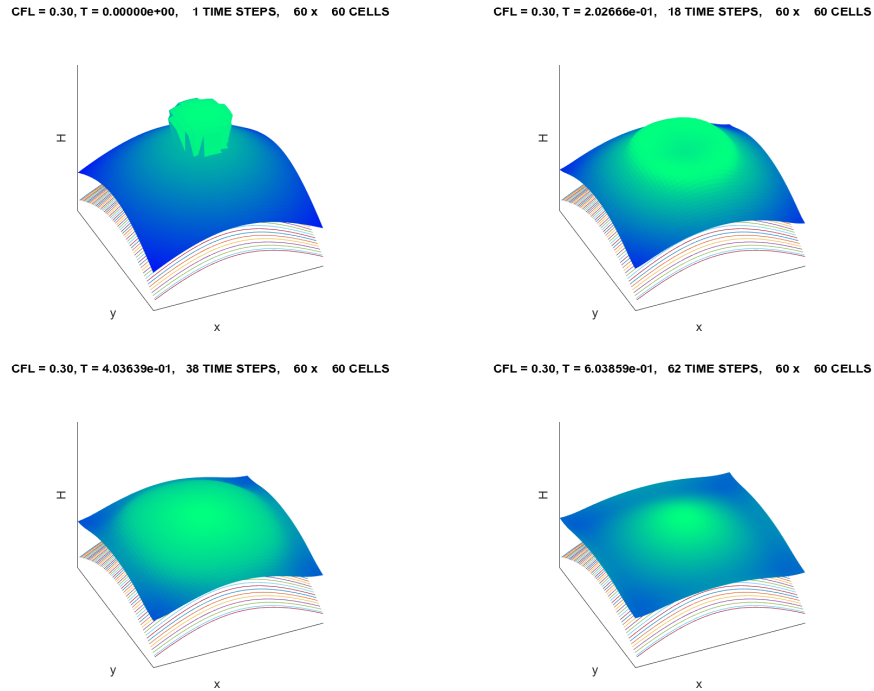


Figure 10: Hyperboloid-central-bump: evolution of the water depth at times $t = 0.0, 0.2, 0.4, 0.6$ s.

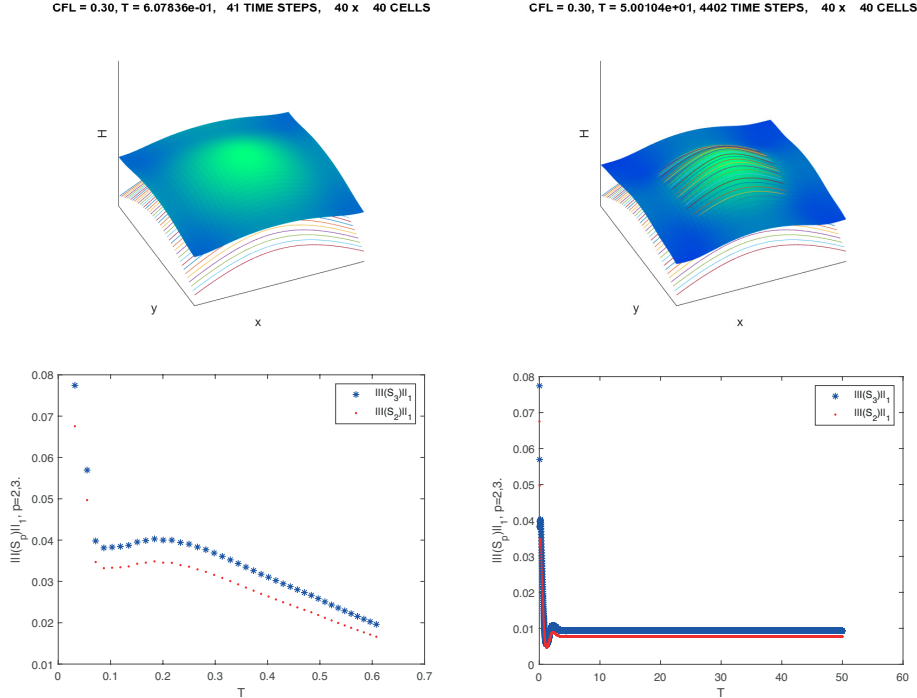


Figure 11: Hyperboloid-central-bump, 40×40 cells: water depth (top panels) and plots of the L^1 -norm of $I(\mathbf{S}^2)$ and $I(\mathbf{S}^3)$ (bottom panels), at times $t = 0.6$ s (left) and $t = 50$ s (right). Computational time for $t = 50$: 6.46 s.

on a domain $U = [-4, 4] \times [-10, 10] \subset \mathbb{R}^2$. The dam is located at $y = -8.5$ m and the initial condition for the depth is set to 2.0 m of water upstream and 1.0 m of water downstream. This is the only example where we used an outlet boundary condition at $y = 10$ m and no-flow conditions for the other boundaries.

Figure 12 shows the evolution of the water depth from the initial solution, $t = 0.0$ s, and at times $t = 0.8$, 1.6, 2.4 s, on a grid that considers 60×600 cells. The long-time numerical tests shown in figure 13 verify the well-balance property of our approach.

Discontinuous initial conditions. Finally, we present a test case in which strongly discontinuous initial conditions are present. The domain is a rectangle $[0, 3] \times [0, 10] \subset \mathbb{R}^2$ and the height function describes a sloping plane, as in the test case 1. We define a dam-break initial condition with a square discontinuity in the central portion of the domain centered at the point $(1.5, 5)$, with support in $\{|x - 1.5| < 0.5\} \cup \{|y - 5| < 0.5\}$, and shape given by the graph of the function $(x - 1.5)^2 + (y - 5)^2 - 0.8$.

Figure 14 shows the evolution of the normal water depth at different times, until the final time $t = 1.10$ s. Again figure 15 reports the long-time simulations that show the robustness over the treatment of the lake-at-rest conditions.

5. Concluding remarks

In this work, we present and discuss a new geometrically intrinsic Lagrangian-Eulerian scheme able to handle non-autonomous fluxes that arise from the spatially varying bottom topography. The scheme is based on the concept of no-flow surfaces that define the integral tube along which the initial value problem is solved. The integral tube is defined by re-writing the ISWE as a time-space divergence of the fluxes that takes into account the intrinsic geometric features of the SW equations, written on a local reference system anchored on the bottom surface. A first Lagrangian evolution step that evolves the solution from time t^n to t^{n+1} along the integral tube is followed by a second Eulerian projection step where the current numerical

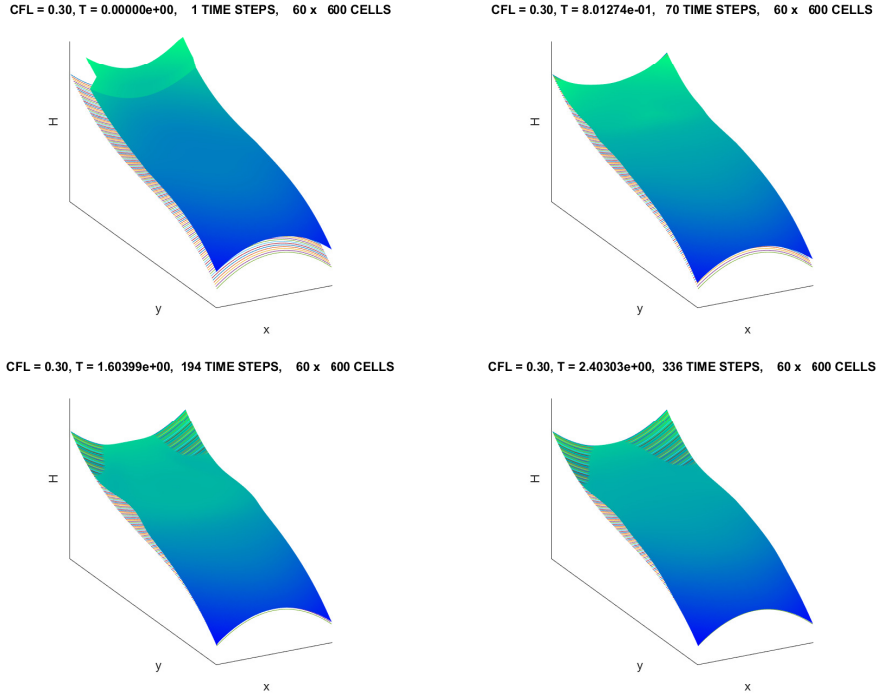


Figure 12: Fully 3D surface: evolution of the water depth at times $T = 0.0, 0.8, 1.6, 2.4$ s.

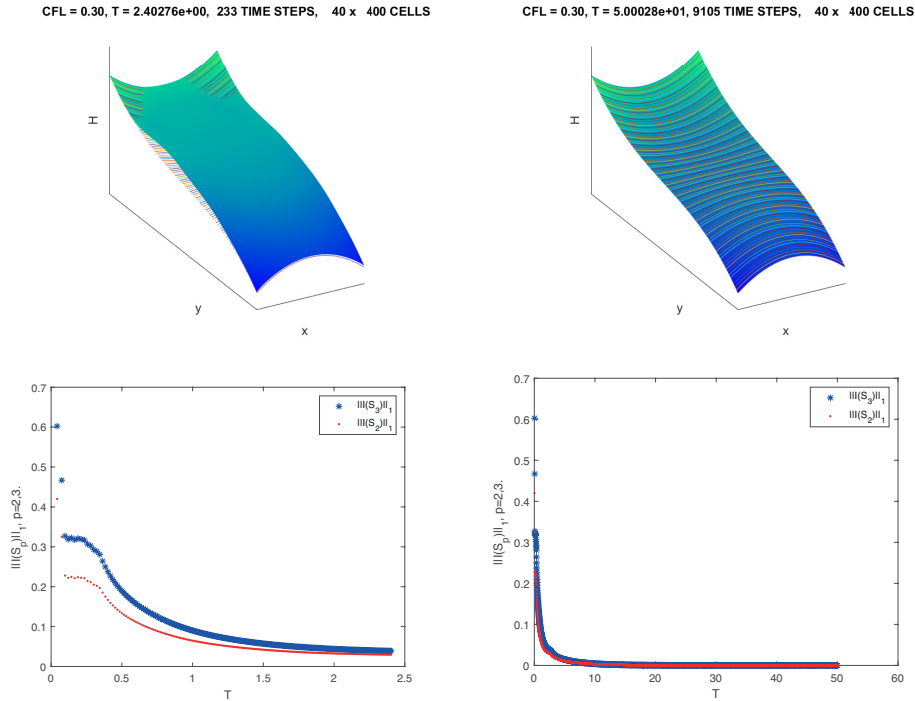


Figure 13: Fully 3D surface, 40x400 cells: water depth (top panels) and plots of the L^1 -norm of $I(\mathbf{S}^2)$ and $I(\mathbf{S}^3)$ (bottom panels), at times $t = 0.6$ s (left) and $t = 50$ s (right). Computational time for $t = 50$: 45.65 s.

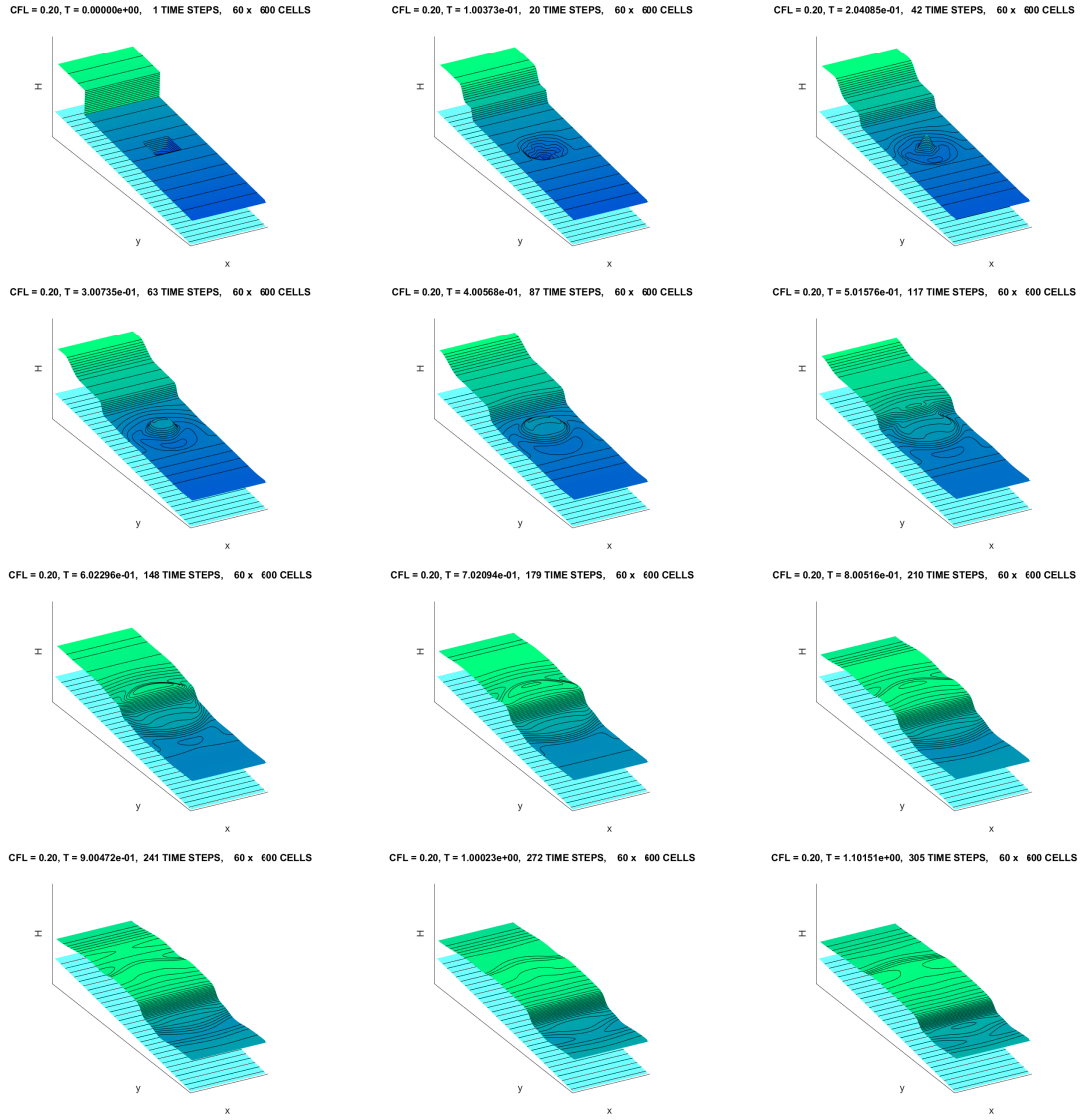


Figure 14: Sloping plane with discontinuous initial data: dam-break problem on a sloping plane with initial condition that are discontinuous in the central portion of the domain. The different frames show the evolution of the water depth from the initial solution, $t = 0.0$ s (top left corner) to a final time of $t = 1.10$ s (bottom right corner).

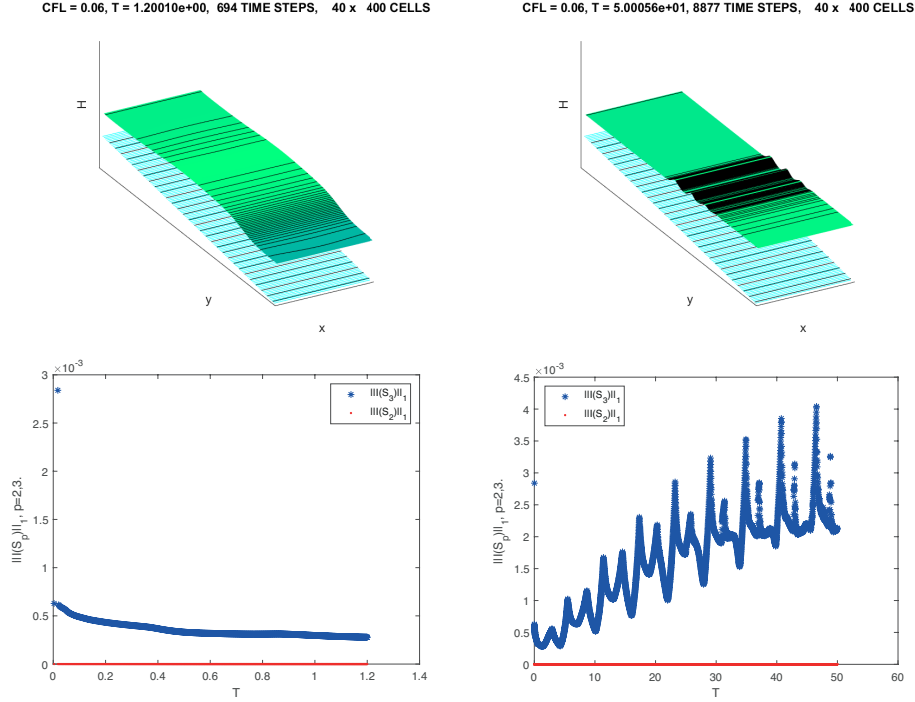


Figure 15: Sloping plane with discontinuous initial datum, 40×400 cells: water depth (top panels) and plots of the L^1 -norm of $I(\mathbf{S}^2)$ and $I(\mathbf{S}^3)$ (bottom panels), at times $t = 1.2$ s (left) and $t = 50$ s (right). Computational time for $t = 50$: 47.04 s.

approximation is averaged over the original grid. The scheme is efficient in terms of computational and memory cost and, at the same time, is easy to implement since no (local) Riemann problems are solved. Moreover, it allows to handle seamlessly the non-autonomous fluxes arising in the ISWE formulation. We show monotonicity and stability of the scheme, provided by a new weak CFL-type constraint. These features are significant and ensure the simplicity and robustness of this class of *no-flow surface* Lagrangian-Eulerian schemes.

This new scheme is also applicable to scalar equations and systems of hyperbolic conservation laws as well as for modeling transport problems in the presence of a general bottom topography with non-negligible slopes and curvatures, such as a mountain landscape. Numerical examples on mountain-like topographies are used to verify the theoretical developments and illustrate the capabilities of the proposed approach in a range of two-dimensional shallow water equations. The results show the robustness of the Lagrangian-Eulerian formulation on Cartesian grids for relatively mild and slowly varying curvatures verifying the ISWE hypothesis.

Acknowledgments

E. Abreu gratefully acknowledges the financial support of the the National Council for Scientific and Technological Development - Brazil (CNPq) (Grant 306385/2019-8). E. Bachini wishes to thank the German Research Foundation (DFG) for financial support within the Research Unit “Vector- and Tensor-Valued Surface PDEs” (FOR 3013) with project no. VO 899/22-1.

Appendix A. Geometrically intrinsic differential operators

We recall here the definition of the intrinsic differential operators taking into account the metric tensor (see [2]). Let (t, s^1, s^2) be the coordinate set of the LCS and $\mathbb{G} = \{g_{ii}\}$ the associated metric tensor. Let $f : \Omega \rightarrow \mathbb{R}$ be a scalar function, $\vec{u} : \Omega \rightarrow \mathbb{R}^3$ a contravariant vector field given by $\vec{u} = u^1 \mathbf{N} + u^2 \mathbf{t}_1 + u^3 \mathbf{t}_2$, and

$\mathbb{T} : \Omega \rightarrow \mathbb{R}^{3 \times 3}$ a rank-2 contravariant symmetric tensor given by $\mathbb{T} = \{\tau^{ij}\}$. Then, the differential operators in the LCS are given by the following expressions:

- the gradient of f is:

$$\nabla_{\mathbb{G}} f = \mathbb{G}^{-1} \nabla f = \left(\frac{\partial f}{\partial t}, \frac{1}{h_{(1)}^2} \frac{\partial f}{\partial s^1}, \frac{1}{h_{(2)}^2} \frac{\partial f}{\partial s^2} \right);$$

- the divergence of \vec{u} is:

$$\nabla_{\mathbb{G}} \cdot \vec{u} = \frac{1}{\sqrt{\det(\mathbb{G})}} \nabla \cdot (\sqrt{\det(\mathbb{G})} \vec{u}) = \frac{1}{h_{(1)} h_{(2)}} \left(\frac{\partial (h_{(1)} h_{(2)} u^1)}{\partial t} + \frac{\partial (h_{(1)} h_{(2)} u^2)}{\partial s^1} + \frac{\partial (h_{(1)} h_{(2)} u^3)}{\partial s^2} \right); \quad (\text{A.1})$$

- the j -th component of the divergence \mathbb{T} is:

$$\begin{aligned} (\nabla_{\mathbb{G}} \cdot \mathbb{T})^j &= \nabla_{e_i} \tau^{ij} = \frac{1}{\sqrt{\det(\mathbb{G})}} \partial_i (\sqrt{\det(\mathbb{G})} \tau^{ij}) + \Gamma_{ik}^j \tau^{ik} = \\ &= \nabla_{\mathbb{G}} \cdot \tau^{(\cdot j)} + \frac{1}{\sqrt{g_{jj}}} \left(2\tau^{1j} \frac{\partial \sqrt{g_{jj}}}{\partial t} - \tau^{11} \frac{\sqrt{g_{11}}}{\sqrt{g_{jj}}} \frac{\partial \sqrt{g_{11}}}{\partial s^j} \right) + \frac{1}{\sqrt{g_{jj}}} \left(2\tau^{2j} \frac{\partial \sqrt{g_{jj}}}{\partial s^1} - \tau^{22} \frac{\sqrt{g_{22}}}{\sqrt{g_{jj}}} \frac{\partial \sqrt{g_{22}}}{\partial s^j} \right) \\ &\quad + \frac{1}{\sqrt{g_{jj}}} \left(2\tau^{3j} \frac{\partial \sqrt{g_{jj}}}{\partial s^2} - \tau^{33} \frac{\sqrt{g_{33}}}{\sqrt{g_{jj}}} \frac{\partial \sqrt{g_{33}}}{\partial s^j} \right) \quad (\text{if } j = 1 \text{ the } s^j = t) \\ &= \nabla_{\mathbb{G}} \cdot \tau^{(\cdot j)} + \frac{1}{\sqrt{g_{jj}}} \left(2\tau^{2j} \frac{\partial \sqrt{g_{jj}}}{\partial s^1} - \tau^{22} \frac{\sqrt{g_{22}}}{\sqrt{g_{jj}}} \frac{\partial \sqrt{g_{22}}}{\partial s^j} \right) + \frac{1}{\sqrt{g_{jj}}} \left(2\tau^{3j} \frac{\partial \sqrt{g_{jj}}}{\partial s^2} - \tau^{33} \frac{\sqrt{g_{33}}}{\sqrt{g_{jj}}} \frac{\partial \sqrt{g_{33}}}{\partial s^j} \right), \quad (\text{A.2}) \end{aligned}$$

where $\nabla_{\mathbb{G}} \cdot \tau^{(\cdot j)}$ identifies the divergence of the j -th column of \mathbb{T} , and Γ_{ij}^k denote the Christoffel symbols.

By applying this definitions, we can prove the equivalence between formulation (1) and (2). Using equation (A.2), the divergence of the tensor $\underline{\underline{F}}$ is given by:

$$\begin{aligned} \text{ROW 1: } (\nabla_{\mathbb{G}} \cdot \underline{\underline{F}})^1 &= \nabla_{\mathbb{G}} \cdot \underline{\underline{F}}^{(\cdot 1)} \\ \text{ROW 2: } (\nabla_{\mathbb{G}} \cdot \underline{\underline{F}})^2 &= \nabla_{\mathbb{G}} \cdot \underline{\underline{F}}^{(\cdot 2)} + \frac{1}{h_{(1)}} F^{21} \frac{\partial h_{(1)}}{\partial s^1} + \frac{1}{h_{(1)}} \left(2F^{31} \frac{\partial h_{(1)}}{\partial s^2} - F^{32} \frac{h_{(2)}}{h_{(1)}} \frac{\partial h_{(2)}}{\partial s^1} \right) \\ \text{ROW 3: } (\nabla_{\mathbb{G}} \cdot \underline{\underline{F}})^3 &= \nabla_{\mathbb{G}} \cdot \underline{\underline{F}}^{(\cdot 3)} + \frac{1}{h_{(2)}} \left(2F^{22} \frac{\partial h_{(2)}}{\partial s^1} - F^{21} \frac{h_{(1)}}{h_{(2)}} \frac{\partial h_{(1)}}{\partial s^2} \right) + \frac{1}{h_{(2)}} F^{32} \frac{\partial h_{(2)}}{\partial s^2} \end{aligned}$$

Applying the definition of the divergence of a vector given in (A.1) to ROW 1 we obtain:

$$\frac{\partial \eta}{\partial t} + \frac{1}{h_{(1)} h_{(2)}} \left(\frac{\partial (h_{(1)} h_{(2)} q^1)}{\partial s^1} + \frac{\partial (h_{(1)} h_{(2)} q^2)}{\partial s^2} \right) = \frac{\partial \eta}{\partial t} + \nabla_{\mathbb{G}} \cdot \vec{q},$$

while for ROWS 2 and 3 we need to apply the expression for the divergence of a tensor (2), obtaining:

$$\frac{\partial \vec{q}}{\partial t} + \nabla_{\mathbb{G}} \cdot \mathbf{F}.$$

These two equations provide the ISWE model (1) in absence of source term.

References

- [1] M. Nestler, I. Nitschke, A. Voigt, A finite element approach for vector- and tensor-valued surface pdes, *J. Comp. Phys.* 389 (2019) 48–61. doi:10.1016/j.jcp.2019.03.006.
- [2] E. Bachini, M. Putti, Geometrically intrinsic modeling of shallow water flows, *Math. Model. Num. Anal.* 54 (6) (2020) 2125–2157. doi:10.1051/m2an/2020031.
- [3] M. P. Neilson, J. A. Mackenzie, S. D. Webb, R. H. Insall, Modeling cell movement and chemotaxis using pseudopod-based feedback, *SIAM J. Sci. Comput.* 33 (3) (2011) 1035–1057.
- [4] J. Lowengrub, J. Allard, S. Aland, Numerical simulation of endocytosis: Viscous flow driven by membranes with non-uniformly distributed curvature-inducing molecules, *J. Comp. Phys.* 309 (2016) 112–128. doi:10.1016/j.jcp.2015.12.055.
- [5] I. Nitschke, A. Voigt, J. Wensch, A finite element approach to incompressible two-phase flow on manifolds, *J. Fluid Mech.* 708 (2012) 418.
- [6] F. Bouchut, M. Westdickenberg, Gravity driven shallow water models for arbitrary topography, *Comm. Math. Sci.* 2 (3) (2004) 359–389.
- [7] A. Decoene, L. Bonaventura, E. Miglio, F. Saleri, Asymptotic derivation of the section-averaged shallow water equations for natural river hydraulics, *Math. Mod. Meth. Appl. Sci.* 19 (03) (2009) 387–417.
- [8] F. Bouchut, S. Boyaval, A new model for shallow viscoelastic fluids, *Math. Mod. Meth. Appl. Sci.* 23 (8) (2013) 1479–1526.
- [9] I. Fent, M. Putti, C. Gregoretto, S. Lanzoni, Modeling shallow water flows on general terrains, *Adv. Water Resour.* 121 (2018) 316–332.
- [10] J. R. Holton, *An introduction to dynamic meteorology*, Burlington, MA: Elsevier Academic Press, 2004.
- [11] R. L. Higdon, Numerical modelling of ocean circulation, *Acta Num.* 15 (2006) 385.
- [12] C. Vreugdenhil, *Numerical Methods for Shallow-Water Flow*, Water Science and Technology Library, Springer Netherlands, 1994.
- [13] L. Bonaventura, E. D. Fernández-Nieto, J. Garres-Díaz, G. Narbona-Reina, Multilayer shallow water models with locally variable number of layers and semi-implicit time discretization, *Journal of Computational Physics* 364 (2018) 209–234.
- [14] R. L. Higdon, An automatically well-balanced formulation of pressure forcing for discontinuous galerkin methods for the shallow water equations, *J. Comp. Phys.* (2022) 111102.
- [15] S. Lanzoni, A. Siviglia, A. Frascati, G. Seminara, Long waves in erodible channels and morphodynamic influence, *Water Resour. Res.* 42 (2006) W06D17.
- [16] R. M. Iverson, D. L. George, A depth-averaged debris-flow model that includes the effects of evolving dilatancy. I. Physical basis, *Proc. R. Soc. London* 470 (2170) (2014) 20130819–20130819.
- [17] S. B. Savage, K. Hutter, The dynamics of avalanches of granular materials from initiation to runout. Part I: Analysis, *Acta Mech.* 86 (1-4) (1991) 201–223.
- [18] J. A. Rossmannith, D. S. Bale, R. J. LeVeque, A wave propagation algorithm for hyperbolic systems on curved manifolds, *J. Comp. Phys.* 199 (2) (2004) 631–662.
- [19] D. S. Bale, R. J. LeVeque, S. Mitran, J. A. Rossmannith, A wave propagation method for conservation laws and balance laws with spatially varying flux functions, *SIAM J. Sci. Comput.* 24 (3) (2003) 955–978.
- [20] B. Andreianov, K. H. Karlsen, N. H. Risebro, On vanishing viscosity approximation of conservation laws with discontinuous flux., *NHM* 5 (3) (2010) pp.617–633. doi:10.3934/nhm.2010.5.617.
- [21] B. Andreianov, K. H. Karlsen, N. H. Risebro, A theory of l^1 -dissipative solvers for scalar conservation laws with discontinuous flux, *Arch. Rational Mech. Anal.* 201 (1) (2011) pp.27–86. doi:10.1007/s00205-010-0389-4.
- [22] X. sun, G. Wang, Y. Ma, A new modified local lax–friedrichs scheme for scalar conservation laws with discontinuous flux, *Appl. Math. Let.* 105 (2020) 106328. doi:10.1016/j.aml.2020.106328.
- [23] D. Qiao, Z. Lin, M. Guo, X. Yang, X. Li, P. Zhang, X. Zhang, Riemann solvers of a conserved high-order traffic flow model with discontinuous fluxes, *Applied Mathematics and Computation* 413 (2022) 126648. doi:10.1016/j.amc.2021.126648.
- [24] F. Bouchut, *Nonlinear Stability of Finite Volume Methods for Hyperbolic Conservation Laws and Well-Balanced Schemes for Sources*, Vol. 2/2004 of *Frontiers in Mathematics*, Birkhäuser Basel, 2004. doi:10.1007/b93802.
- [25] E. Bachini, Numerical methods for shallow water equations on regular surfaces, Ph.D. thesis, Department of Mathematics “Tullio Levi-Civita”, Doctoral Program in Mathematics, University of Padua, Italy (2020).
- [26] E. F. Toro, A. Hidalgo, M. Dumbser, Force schemes on unstructured meshes i: Conservative hyperbolic systems, *J. Comp. Phys.* 228 (9) (2009) 3368–3389. doi:10.1016/j.jcp.2009.01.025.
- [27] E. Abreu, J. Pérez, A fast, robust, and simple Lagrangian–Eulerian solver for balance laws and applications, *Comput. Math. Appl.* 77 (9) (2019) 2310–2336.
- [28] E. Abreu, W. Lambert, J. Perez, A. Santo, A new finite volume approach for transport models and related applications with balancing source terms, *Math. Comp. Simul.* 137 (2017) 2–28.
- [29] E. Abreu, J. Pérez, A. Santo, Lagrangian–Eulerian approximation methods for balance laws and hyperbolic conservation laws, *Rev. UIS Ing.* 17 (1) (2018) 191–200.
- [30] E. Abreu, J. Pérez, A. Santo, A conservative Lagrangian–Eulerian finite volume approximation method for balance law problems, *Proc. Ser. Braz. Soc. Comput. Appl. Math.* 6 (1) (2018).
- [31] E. Abreu, C. Diaz, J. Galvis, J. Pérez, On the conservation properties in multiple scale coupling and simulation for darcy flow with hyperbolic-transport in complex flows, *Multiscale Model. Simul.* 18 (4) (2020) 1375–1408.
- [32] E. Abreu, V. Matos, J. Pérez, P. Rodríguez-Bermúdez, A class of Lagrangian–Eulerian shock-capturing schemes for first-order hyperbolic problems with forcing terms, *J. Scient. Comput.* 86 (1) (2021) 1–47.
- [33] A. Bressan, M. Lewicka, W. Dehua, Y. Zheng (Eds.), *A weak asymptotic solution analysis for a Lagrangian–Eulerian scheme for scalar hyperbolic conservation laws*, Vol. 1, 2020.

- [34] J. Pérez, Lagrangian-Eulerian approximation methods for balance laws and hyperbolic conservation laws, Ph.D. thesis, University of Campinas (2015).
- [35] C.-S. Huang, T. Arbogast, C.-H. Hung, A semi-lagrangian finite difference weno scheme for scalar nonlinear conservation laws, *Journal of Computational Physics* 322 (2016) 559–585.
- [36] R. Loubere, P.-H. Maire, M. Shashkov, J. Breil, S. Galera, Reale: A reconnection-based arbitrary-lagrangian–eulerian method, *Journal of Computational Physics* 229 (12) (2010) 4724–4761.
- [37] J. Douglas, F. Pereira, L.-M. Yeh, A locally conservative eulerian–lagrangian numerical method and its application to nonlinear transport in porous media, *Computational Geosciences* 4 (1) (2000) 1–40.
- [38] J. Douglas, F. Pereira, L.-M. Yeh, A locally conservative eulerian-lagrangian method for flow in a porous medium of a mixture of two components having different densities, in: *Numerical Treatment of Multiphase Flows in Porous Media*, Springer, 2000, pp. 138–155.
- [39] J. Douglas, C.-S. Huang, A locally conservative eulerian-lagrangian finite difference method for a parabolic equation, *BIT Numerical Mathematics* 41 (3) (2001) 480–489.
- [40] J. Aquino, A. Francisco, F. Pereira, T. J. Pereira, H. A. Souto, A lagrangian strategy for the numerical simulation of radionuclide transport problems, *Progress in Nuclear Energy* 52 (3) (2010) 282–291.
- [41] J. Douglas, F. Pereira, L.-M. Yeh, A locally conservative Eulerian–Lagrangian numerical method and its application to nonlinear transport in porous media, *Comput. Geosci.* 4 (1) (2000) 1–40.
- [42] E. Abreu, J. François, W. Lambert, J. Pérez, A semi-discrete Lagrangian–Eulerian scheme for hyperbolic-transport models, *J. Comput. Appl. Math.* 406 (2022) 114011.
- [43] E. Abreu, J. Perez, A. Santo, Solving hyperbolic conservation laws by using Lagrangian-Eulerian approach, in: *Proceeding Series of the Brazilian Society of Applied and Computational Mathematics*, Vol. 5, 2017.
- [44] R. J. Leveque, *Finite Volume Methods for Hyperbolic Problems*, Cambridge University Press, Trumpington Street, Cambridge, UK, 2002.
- [45] C. Chainais-Hillairet, Finite volume schemes for a nonlinear hyperbolic equation. convergence towards the entropy solution and error estimate, *Math. Model. Num. Anal.* 33 (1) (1999) 129–156.
- [46] R. Eymard, T. Gallouët, R. Herbin, Convergence of a finite volume scheme for a nonlinear hyperbolic equation, in: *Proceedings of the Third International Colloquium on Numerical Analysis*, (Plovdiv, 1994)(Utrecht), VSP, 1995, pp. 61–70.
- [47] R. Eymard, T. Gallouët, R. Herbin, Existence and uniqueness of the entropy solution to a nonlinear hyperbolic equation, *Chin. Ann. Math B* 16 (1995) 1–14.
- [48] M. G. Crandall, A. Majda, Monotone difference approximations for scalar conservation laws, *Math. Comp.* 34 (149) (1980) 1–21.
- [49] T. Barth, R. Herbin, M. Ohlberger, *Finite Volume Methods: Foundation and Analysis*, John Wiley & Sons, Ltd, 2017, pp. 1–60. doi:10.1002/9781119176817.ecm2010.
- [50] E. Abreu, J. François, W. Lambert, J. Pérez, A class of positive semi-discrete Lagrangian–Eulerian schemes for multidimensional systems of hyperbolic conservation laws, *J. Scient. Comput.* 90 (1) (2022) 1–79.